

1 **Quantifying errors in surface ozone predictions associated**
2 **with clouds over CONUS: A WRF-Chem modeling study**
3 **using satellite cloud retrievals**

4 **Young-Hee Ryu¹, Alma Hodzic^{1,2,*}, Jerome Barre^{1,a}, Gael Descombes¹, Patrick Minnis³**

5

6 *¹National Center for Atmospheric Research, Boulder, CO, USA*

7 *²Laboratoire d'Aérodologie, Observatoire Midi-Pyrénées, CNRS, Toulouse, France.*

8 *³NASA Langley Research Center, Hampton, VA, USA*

9 *^anow at: European Centre for Medium-Range Weather Forecasts, Reading, United Kingdom*

10 *^{1,*}Correspondence to A. Hodzic: alma@ucar.edu*

11

12

13

14

15

16 ***Key words: surface ozone, photolysis, satellite clouds, WRF-Chem***

17

18
19
20
21
22
23
24
25
26
27
28
29
30
31
32
33
34
35
36
37
38
39

Abstract

Clouds play a key role in radiation and hence O₃ photochemistry by modulating photolysis rates and light-dependent emissions of biogenic volatile organic compounds (BVOCs). It is not well known, however, how much error in O₃ predictions can be directly attributed to error in cloud predictions. This study applies the Weather Research and Forecasting with Chemistry (WRF-Chem) at 12 km horizontal resolution with the Morrison microphysics and Grell 3D cumulus parameterization to quantify uncertainties in summertime surface O₃ predictions associated with the cloudiness over contiguous United States (CONUS). All model simulations are driven by reanalysis of atmospheric data and reinitialized every 2 days. In sensitivity simulations, cloud fields used for photochemistry are corrected based on satellite cloud retrievals. The results show that WRF-Chem predicts about 55% of clouds in the right locations and generally underpredicts cloud optical depths. These errors in cloud predictions can lead up to 60 ppb overestimation in hourly surface O₃ concentrations on some days. The average difference in summertime surface O₃ concentrations derived from the modeled clouds and satellite clouds ranges from 1 to 5 ppb for maximum daily 8-h average O₃ (MDA8 O₃) over CONUS. This represents up to ~40% of the total MDA8 O₃ bias under cloudy conditions in the tested model version. Surface O₃ concentrations are sensitive to cloud errors mainly through the calculation of photolysis rates (for ~80%), and to a lesser extent to light-dependent BVOC emissions. The sensitivity of surface O₃ concentrations to satellite-based cloud corrections is about 2 times larger in VOC-limited than NO_x-limited regimes. Our results suggest that the benefits of accurate predictions of cloudiness would be significant in VOC-limited regions which are typical of urban areas.

40 **1. Introduction**

41 Ozone (O₃) is a secondary pollutant that is formed by chemical reactions involving nitrogen
42 oxides (NO_x = NO + NO₂) and volatile organic compounds (VOCs) in the presence of ultraviolet
43 radiation. Because O₃ is a harmful pollutant and a greenhouse gas, there have been numerous
44 efforts aimed at improving O₃ predictions in air quality models, i.e. through a better
45 characterization of the emissions of O₃ precursors (Brioude et al., 2013), more detailed chemical
46 mechanisms (Carter, 2010; Sarwar et al., 2013), more realistic lateral boundary conditions (e.g.,
47 Tang et al., 2009), and improved representation of meteorological fields with ensemble modeling
48 techniques (Bei et al., 2010; Zhang et al., 2007). A comprehensive review of the current status
49 and challenges of air quality forecasting is given by Zhang et al. (2012). A large O₃ bias that still
50 persists in most regional and global models is one of the challenges (Brown-Steiner et al., 2015;
51 Fiore et al., 2009; Im et al., 2015; Lin et al., 2017; Travis et al., 2016). The recent multi-model
52 intercomparison study by Im et al. (2015) indicates that over North America models tend to
53 overestimate hourly surface O₃ below 30 ppb by 15–25% and to underestimate O₃ levels above
54 60 ppb by up to ~80%. It is not quantitatively understood how much the individual processes
55 contribute to O₃ biases. Among meteorological parameters, clouds can be one of the key factors
56 because they greatly modulate the ultraviolet radiation that is critical for O₃ formation. However,
57 they remain one of the largest sources of uncertainties in air quality modeling as Dabberdt et al.
58 (2004) pointed out a decade ago. Accurate cloud predictions in numerical weather models are
59 still challenging, and it has not yet been quantified how much errors in cloud prediction impact
60 surface O₃ predictions.

61 As satellite cloud products have emerged, providing reasonably accurate data with wide
62 coverage and high temporal resolutions in near-real time (e.g., Minnis et al., 2008), they have

63 been employed in various studies to quantify the effects of clouds on actinic fluxes and/or
64 photolysis rates (Mayer et al., 1998; Ryu et al., 2017; Thiel et al., 2008). Clouds can greatly
65 reduce or enhance actinic flux below, above, and inside clouds, and these effects depend mainly
66 on the cloud optical properties. Ryu et al. (2017) used satellite cloud retrievals of cloud bottom
67 and top heights and cloud optical depth (COD) in a radiative transfer model, and showed that one
68 can obtain fairly good (within $\pm 10\%$) vertical distributions of cloudy-sky actinic flux using
69 satellite cloud properties. There are, however, only a limited number of studies that have
70 examined the impact of satellite-constrained clouds and photolysis rates on O₃ formation. Pour-
71 Biazar et al. (2007) and Tang et al. (2015) used satellite-observed clouds to correct photolysis
72 rates in a three-dimensional chemistry transport model and reported considerable improvement
73 in surface O₃ simulations. Pour-Biazar et al. (2007) showed that the difference in O₃ due to the
74 errors in cloud predictions can be up to 60 ppb for a given pollution episode over the south US.
75 Tang et al. (2015) showed that 1-month averages of 8-h surface O₃ can differ by 2–3 ppb
76 between the simulations using satellite-derived clouds and model-predicted clouds over the south
77 US. These studies were performed for rather short time periods (a week or a month) over limited
78 areas, and provide motivation for a more systematic/comprehensive quantification of the
79 importance of cloud errors in O₃ predictions in summertime and for various chemical regimes.

80 In the present study, we use satellite-derived COD and cloud boundaries to constrain radiation
81 fields that impact photochemistry, i.e., photolysis rates and light-dependent BVOC emissions, in
82 a three-dimensional chemistry transport model (WRF-Chem). Our study targets the contiguous
83 United States (CONUS) and numerical simulations are performed for June–September 2013. The
84 WRF-simulated clouds are first evaluated against the Geostationary Operational Environmental
85 Satellite (GOES) data (section 3). The vertical profiles of NO₂ photolysis rates are evaluated

86 against in-situ airborne measurements during two field campaigns (section 4). The O₃ biases
87 arising from inaccurate cloud predictions are quantified, and discussed in light of the sensitivity
88 of O₃ chemistry to COD (section 5). Unlike the previously mentioned studies, here we quantify
89 separately the contributions of errors arising from changes in photolysis rates altered by clouds
90 vs. those arising from light-dependent BVOC emissions to the O₃ biases. Conclusions and
91 discussion are given in section 6.

92 **2. Methodology**

93 **2.1. Satellite retrievals**

94 The GOES retrievals were performed using the Satellite CLOUD and Radiation Property Retrieval
95 System (SatCORPS), which is an adaptation of the Minnis et al. (2011) algorithms for
96 application to imagers on all geostationary weather satellites (Minnis et al. 2008) and on NOAA
97 and MetOp satellites (Minnis et al. 2016). For SatCORPS, the algorithms of Minnis et al. (2011)
98 were altered as described by Minnis et al. (2010) using the low-cloud height estimation method
99 of Sun-Mack et al. (2014) and the severely roughened hexagonal column optical model of Yang
100 et al. (2008) for ice cloud COD retrievals. This study uses a subset of the hourly, 8-km
101 SatCORPS cloud retrievals from GOES 13 (GOES-East) and GOES 15 (GOES-West) for the
102 North American domain. The 8-km resolution is achieved by analyzing only every other 4-km
103 pixel and line. Each pixel is considered to be either 100% cloudy or 100% clear. Of the variety of
104 cloud properties available, this study only uses cloud bottom height, cloud top height, and COD.
105 Uncertainties in the cloud products are summarized by Ryu et al. (2017).

106 Images from coincident times were unavailable for the two satellites: the GOES 13 and GOES
107 15 data are offset by 15 min. The GOES 13 data taken at UTC + 45 min at every hour were

108 matched with the GOES 15 data at UTC + 00 min. The pixel-level retrievals were re-gridded to a
109 12-km resolution to match the WRF-Chem domain (see section 2.2) using the Earth System
110 Modeling Framework (ESMF) software and the nearest-neighbor interpolation. Because of the
111 coverage difference between the two satellites, the data of the nearest time from the two satellites
112 (e.g., 1845 UTC from GOES 13 and 1900 UTC from GOES 15) are merged at 105°W, which is
113 equidistant from the two sub-satellite longitudes. Only daytime hours (09–23 UTC and 00–04
114 UTC) are used here.

115

116 **2.2. WRF-Chem model simulations**

117 The present study employs the WRF-Chem model version 3.6.1. with the updated photolysis
118 scheme. A single domain is used with a horizontal grid size of 12 km (Fig. 1). The
119 meteorological initial and boundary conditions are provided by the NCEP FNL (Final)
120 Operational Global Analysis data with a horizontal resolution of 1°, which are available every 6
121 hours. The model is initialized at 00 UTC 1 June 2013 and spun-up for the first 10 days in the
122 control simulation (CNTR simulation). The meteorological fields are re-initialized every 48
123 hours at 06 UTC of a given day to avoid the growth of model errors, and the model is run for 54
124 hours. Here, the first 6 hours are allowed for spin-up and discarded in each run. The model
125 outputs for the period of 12 UTC 11 June 2013 through 12 UTC 1 October 2013 are used for the
126 analysis. As the goal of the study is to use and evaluate the modeled clouds and their impact on
127 O₃ predictions, nudging is not used. This is different from many previous air quality studies that
128 nudged the meteorology and evaluated modeled O₃ with observations. The physics options used
129 are the Morrison two-moment scheme (Morrison et al., 2009) for the microphysics, RRTMG
130 scheme for longwave and shortwave radiation (Iacono et al., 2008), MYNN 2.5 level TKE

131 scheme for the boundary layer parameterization (Nakanishi and Niino, 2006), MYNN surface
132 layer scheme, Noah land surface model (Chen and Dudhia, 2001), and Grell 3D ensemble
133 scheme (Grell and Devenyi, 2002) for cumulus parameterization with radiation feedback. The
134 initial and boundary conditions for chemical species are obtained from the Model for OZone And
135 Related chemical Tracers (MOZART) global simulation of trace gases and aerosols. For each 2-
136 day simulation, the chemical state of the atmosphere at 06 UTC is obtained from that at 06 UTC
137 of the previous simulation. The MOZART-4 mechanism is used for gas-phase chemistry as
138 described in Knote et al. (2014), and the Model for Simulating Aerosol Interaction and
139 Chemistry (MOSAIC) aerosol module with 4 bins is used for the aerosol chemistry.
140 Anthropogenic gas and aerosol emissions are adopted from the AQMEII project in which the
141 emissions were projected to 2010 from the NEI 2008 inventory (Campbell et al., 2015). Since
142 Travis et al. (2016) reported that NEI NO_x emissions are too high, we reduced NO_x emission
143 from all anthropogenic sources by 40% based on their analysis. Note that the NO_x and PAN
144 from the lateral boundaries are also reduced by 40% in our study. Biomass burning emissions are
145 taken from the Fire Inventory from NCAR (FINN) (Wiedinmyer et al., 2011). Model of
146 Emissions of Gases and Aerosols from Nature (MEGAN) (Guenther et al., 2006) version 2.04 is
147 used for BVOC emissions. As done in Travis et al. (2016) to better match isoprene flux
148 observations during the Studies of Emissions and Atmospheric Composition, Clouds and Climate
149 Coupling by Regional Surveys (SEAC⁴RS) field campaign (Toon et al., 2016), we reduced
150 MEGAN isoprene emissions by 15% over the southeast US. The photolysis rate calculations
151 utilize the newly implemented TUV option in the WRF-Chem model (Hodzic et al., 2017 in
152 preparation). This new TUV option uses the updated cross section and quantum yield data based
153 on the latest stand-alone TUV model version 5.3, and considers 156 wavelength bins with the

154 resolutions of 1–5 nm. The COD is calculated based on the parameterization given in Chang et al.
155 (1987), which uses cloud liquid water and/or ice water contents and effective droplet radius
156 (assumed to be 10 μm both for liquid and ice droplets). To represent subgrid cloud overlaps, a
157 simple equation of Briegleb (1992) is used, i.e., the effective $\text{COD} = \text{COD}_0 \times (\text{cloud fraction})^{1.5}$,
158 where COD_0 is the cloud optical depth that is calculated following Chang et al. (1987), and the
159 cloud fraction is determined based on the relative humidity in a given grid box. According to
160 Briegleb (1992), applying a power of 1.5 to the cloud fraction is equivalent to the maximum
161 random overlap.

162 In the present study, we performed two sets of simulations that use WRF generated clouds in the
163 CNTR simulation and the GOES clouds in the GOES simulation. The GOES simulations are
164 conducted from 06 UTC 11 June 2013 through 12 UTC 1 October 2013. The initial chemistry
165 conditions in the GOES simulation are adopted from the outputs of the CNTR simulation at 06
166 UTC 11 June 2013. The satellite cloud retrievals are used only to correct photolysis rate and
167 photosynthetically active radiation (PAR) calculations (i.e., only within the TUV model in WRF-
168 Chem). That is, the satellite cloud information is not linked to dynamics, microphysics, and
169 atmospheric radiation. The value of COD is linearly distributed through vertical grids from the
170 cloud bottom to the cloud top within the TUV model as done in Ryu et al. (2017). This method is
171 different from the one used in Pour-Biazar et al. (2007) and Tang et al. (2015) in which cloud
172 bottom height used in their photolysis rate calculations is estimated from the meteorological
173 model rather than retrieved from the satellite. The use of model estimates can lead to additional
174 uncertainties in the case of misplaced model clouds compared to observations.

175 In the present study, PAR calculated from the TUV model is used for the BVOC emissions in
176 MEGAN for all simulations. This is different from the PAR conventionally used in MEGAN,

177 which is simply converted/scaled from the downward shortwave radiation from the atmospheric
178 radiation scheme. In the CNTR (GOES) simulation, the WRF generated clouds (GOES clouds)
179 are used for the PAR calculation within the TUV model.

180 To examine the impact of changes in BVOC emissions on surface O₃, another set of sensitivity
181 simulation (EMIS_BVOC simulation) is performed for 10 days (3–12 July 2013), which uses
182 WRF-generated clouds for the PAR calculation and BVOC emissions as in the CNTR simulation
183 but uses the GOES clouds for photolysis rate calculations as in the GOES simulation. The
184 description of the control and sensitivity simulations is summarized in Table 1.

185

186 **2.3. Observational data**

187 *2.3.1. Aircraft data from field campaigns*

188 We evaluate the model performance using airborne measurements made during two field
189 campaigns in 2013, i.e., the NOMADSS (Nitrogen, Oxidants, Mercury and Aerosol Distributions,
190 Sources and Sinks) and the SEAC⁴RS campaigns. The detailed description of the instrument and
191 measurement data is given in Ryu et al (2017). The NOMADSS campaign was conducted during
192 1 June–15 July 2013 mainly over the southeast US. We use 16 flight-day data at 1-min time
193 intervals for the analysis. Data with solar zenith angles larger than 85° are not used. The fire
194 plume data are filtered out by excluding the data showing NO₂ (> 0.1 ppb) or CO (> 120 ppb)
195 aloft at 4–7 km level. Based on the GOES cloud data, 68% of flight data are characterized by
196 clear skies and the remaining data (32%) had clouds in the vertical column where the airplane
197 was located. The SEAC⁴RS campaign also targeted the southeast US although the airplane
198 sometimes flew over a larger region including California and Midwestern US. The period used

199 for the analysis is from 6 August through 23 September 2013, which includes 21 flight days. The
200 time intervals are also 1-min and the data with large solar zenith angles ($> 85^\circ$) and fire plumes
201 are filtered out. The fraction of data with clouds is 41% for SEAC⁴RS. It is noteworthy that
202 SEAC⁴RS measurements include large and thick clouds in some cases as a few of the campaign
203 goals are to identify the role of deep convection in redistributing pollutants and aerosol-clouds
204 feedbacks, whereas the clouds during NOMADSS were mostly broken clouds.

205 *2.3.2. Ground ozone data*

206 The United States Environmental Protection Agency (EPA) hourly O₃ measurements are used for
207 the analysis. To examine the sensitivity of O₃ to COD in different chemical regimes, the VOC-
208 and NO_x-limited regimes are identified using the ratio of $\Delta O_3/\Delta NO_y$, following Sillman and He
209 (2002). They reported that the NO_x-VOC transition occurs when $\Delta O_3/\Delta NO_y = 4-6$. Thus, an
210 EPA site is denoted as a VOC-limited (NO_x-limited) regime when the ratio is less than 4 (greater
211 than 6). Examples showing the ratio of $\Delta O_3/\Delta NO_y$ for several sites are given in the
212 supplementary materials (Fig. S1). Among 1,299 EPA sites, 1,062 are used for the analysis: 24%
213 of the sites are in the VOC-limited and 76% in NO_x-limited regimes. The remaining 237 sites are
214 not used in the present study because those sites fall into the transitional zone, i.e., $\Delta O_3/\Delta NO_y =$
215 4–6. Note that modeled O₃ and NO_y in the CNTR simulation are used to determine whether an
216 EPA site is in VOC-limited or NO_x-limited regime because NO_y measurements are available for
217 limited sites.

218 **3. Evaluation of WRF clouds with satellite measurements**

219 The model bias in the cloud spatial coverage is evaluated using a 2×2 contingency table (Table
220 2), where A and D correspond to hit and correct negative events, respectively, and B and C to

221 false alarm and miss events, respectively. Here, a threshold of 0.3 in hourly COD is used to
222 distinguish between clear and cloudy sky as the lowest detection limit of satellite retrieved COD
223 over land is estimated to 0.25 in Rossow and Schiffer (1999), and the use of 0.3 poses slightly
224 stricter conditions for cloudiness. The agreement index, which is defined as $A+D$ (WRF predicts
225 correctly cloudy or clear skies), is 69.7% and the probability of detection (POD) for clouds,
226 $A/(A+C)$, is 55.6%. It is found that the fraction of errors in missing clouds (C, 19.8%) is larger
227 than that of predicting clouds that are not present in reality (B, 10.4%). The overall bias,
228 $(A+B)/(A+C)$, is 0.789 and this means that the WRF underestimates the frequency of cloudy
229 skies. Figure 1 shows the spatial distribution of each contingency category over the CONUS
230 averaged over the whole study period. In general, the eastern US shows higher cloud frequencies
231 than the western US except for parts of the Rocky Mountains and the Pacific Northwest. The
232 largest agreement index appears in central California where the sky condition is mostly clear (Fig.
233 1d). In terms of errors, the missing clouds rate has its highest frequency (20–35%) in the
234 Midwestern and northwestern US, while the highest frequency of false alarm (20–30%) occurs
235 over the southeast US and the southeastern Texas. The sum of category B and C can be found in
236 the supplementary material (Fig. S2). It should be noted that the contingency categories are
237 based on binary results of cloud-free or cloudiness and so they do not provide quantitative
238 comparison of cloud optical properties, e.g., COD. For example, even though the WRF model
239 produces clouds in the right locations (category A), the WRF CODs can differ from those
240 retrieved from satellite data.

241 Figure 2 evaluates quantitatively COD and vertical extent of clouds between the model and
242 satellite retrievals. The vertical extent of clouds is classified based on the International Satellite
243 Cloud Climatology Project (ISCCP) definition (Rossow and Schiffer, 1999), which are as

244 follows: i) low-level: cloud top height ≤ 3 km, ii) mid-level: $3 \text{ km} < \text{cloud top height} \leq 6$ km, iii)
245 high-level: cloud bottom height > 6 km, and iv) multi-layered or deep convection: cloud bottom
246 height ≤ 6 km and cloud top height > 6 km. Even though multiple cloud layers can be resolved in
247 the WRF model, these kinds of clouds are not resolved in the satellite retrievals used in this study.
248 Thus, for a fair comparison, the multi-layered clouds in the WRF model are not further resolved
249 into cloud layers. Note that the liquid/ice water contents from cumulus clouds (parameterized
250 clouds) are included in the model COD calculations.

251 The frequency distribution of CODs does not have the same shape in the model and observations.
252 The WRF model overpredicts by a factor of 2 very thin clouds with $\text{COD} < 1$, whereas the
253 GOES retrievals show that the most abundant clouds have CODs of 2–5. The majority of
254 optically very thin clouds from the WRF model correspond to high-level cirrus clouds. This is
255 consistent with the result of Cintineo et al. (2013), showing that the Morrison microphysics
256 scheme produces too many upper-level clouds by comparing GOES infrared brightness
257 temperature with the WRF model. Note that the optically-thin multi-layered clouds very likely
258 contain cirrus clouds because their top height is greater than 6 km. The WRF model produces
259 fewer clouds with $\text{COD} > 1$ than observed, and the discrepancy is most apparent for optically
260 very-thick clouds ($\text{COD} > 50$). As a result, the model COD mean and standard deviation are
261 smaller than those for the retrievals, which are 8.3 and 12.7, respectively for the WRF model,
262 and 17.8 and 30.8, respectively for the GOES retrievals.

263 **4. Impact of cloud errors on photolysis rates**

264 Figure 3 compares the cloudy-sky averaged vertical profiles of NO_2 photolysis rates ($J\text{NO}_2$)
265 predicted by WRF-Chem and measured during the NOMADSS (Fig. 3a) and SEAC⁴RS (Fig. 3d)

266 campaigns. The histograms of ratio of JNO₂ simulated to that observed under cloudy conditions
267 are also shown for the CNTR and GOES simulations.

268 For both campaigns, the simulations with satellite clouds (GOES simulations) generally show
269 better agreement with the observed JNO₂ profiles than the CNTR simulations, especially above
270 the boundary layer (above ~2 km). The histograms of the ratio model-to-observation JNO₂ also
271 show a better performance generally in the GOES simulation than in the CNTR simulation: the
272 mean of the ratio is closer to 1 in the GOES simulation than in the CNTR simulation for
273 SEAC⁴RS, the standard deviations are reduced in the GOES simulation compared to those in the
274 CNTR simulation for both campaigns, the root-mean-square-errors are lowered in the GOES
275 simulation compared to those in the CNTR simulation, and the correlation coefficients are closer
276 to 1 in the GOES simulation than in the CNTR simulation. For NOMADSS, the large bias in the
277 highest ratio bin (> 2) is 24% less in the GOES simulation than in the CNTR simulation. The
278 reduction of the large bias (bin > 2) in the GOES simulation is more substantial for SEAC⁴RS
279 and reaches 47%. These reductions are attributed to a better representation of the below-cloud
280 and inside-cloud conditions when satellite clouds are used (not shown). This is because the
281 number of data influenced by thick clouds is larger in SEAC⁴RS than in NOMADSS and the
282 measurements in the presence of those thick clouds were mostly made under below-cloud or
283 inside-cloud conditions.

284 **5. Impact of cloud errors on ground level ozone**

285 **5.1. An example on 8 July 2013 in Midwestern US**

286 Figure 4 shows an example of how model errors in cloud fields impact O₃ predictions. This
287 example includes thunderstorm systems over the Midwestern US. The CNTR simulation misses

288 clouds or underpredicts CODs over metropolitan Chicago and the region south of Lake Michigan.
289 This results in the overprediction of JNO_2 by up to 0.54 min^{-1} (~90%) compared to that
290 computed using GOES clouds. The resulting changes in O_3 concentration are regional and the O_3
291 overprediction in the plume originating from the Chicago area is up to 62 ppb (~60% of O_3 in the
292 CNTR simulation). As a result of the cloud corrections, O_3 in the GOES simulation agrees better
293 with observations in those regions (compare Fig. 4d with Fig. 4e and Figs. 4g,h,i). The time
294 series of O_3 at the three sites (marked in Fig. 4f) near Lake Michigan show particularly improved
295 agreement with observations when satellite clouds are used. The large O_3 biases of 20.5 ppb at
296 11 CST at Chicago, IL, 19.2 ppb at 13 CST at La Porte, IN, and 23.5 ppb at 16 CST at Holland,
297 MI in the CNTR simulation are reduced to 1.7 ppb, 3.2 ppb, and -0.11 ppb in the GOES
298 simulation, respectively. It is also apparent that the bias reduction in O_3 shifts eastward (from
299 Chicago, IL to Holland, MI) as the thunderstorm moves eastward during the day. An important
300 implication of this finding is that errors in cloud predictions can lead to wrong O_3 alerts in areas
301 where model does not predict clouds well. For example, the maximum daily 8-h average O_3
302 (MDA8 O_3) concentration is 75.3 ppb at Holland, MI in the CNTR simulation (Fig. 4i) and this
303 value exceeds the O_3 standard (70 ppb for MDA8 O_3). However, the MDA8 O_3 concentration at
304 the same location is 63.0 ppb in the GOES simulation and 60.4 ppb in the observation. Therefore,
305 an O_3 action alert would have been issued if the CNTR simulation results are used, which results
306 in a false alarm. The example shown here emphasizes the important roles of clouds in the Great
307 Lakes region where large O_3 biases have been reported previously in air quality forecasts (e.g.,
308 Cleary et al., 2015). The correction of clouds both over the lakes and in the upstream regions
309 (mostly large cities located to the west/southwest of the lakes) significantly reduces the O_3 bias.
310 It is also shown that polluted air masses from the source regions can be advected over the lakes

311 (not shown). In this case in which precursor levels can be high over the lakes, the presence of
312 clouds over the lakes can greatly affect O₃ formation over the lakes.

313 In general, the regions exhibiting O₃ differences between the two simulations coincide with the
314 regions where JNO₂ values are different. More importantly, large O₃ differences are found near
315 urban areas (e.g., Chicago, IL; downwind area of Kansas City, MO; Omaha, NE and its
316 downwind area). Even though the difference in COD or JNO₂ is significant in central Indiana,
317 for example, the difference in O₃ in the region is relatively small compared to that near Lake
318 Michigan.

319

320 **5.2. Maximum daily 8-h average O₃**

321 Figure 5 shows the maps of MDA8 O₃ averaged over the study period for the CNTR simulation
322 and the difference in MDA8 O₃ between the CNTR and GOES simulations. The spatial
323 distribution of MDA8 O₃ in the GOES simulation is similar to that in the CNTR simulation (thus
324 the GOES spatial average is not shown here), but the O₃ levels are considerably different. In Fig.
325 5b, the Midwestern, eastern, and northwestern US regions show the largest O₃ differences, up to
326 5.8 ppb, with lower O₃ levels in the GOES simulation. These regions generally belong to the
327 contingency category C (Midwestern and northwestern US) or category A (eastern US). On the
328 other hand, the regions with negative differences, i.e., some places over the south/southeastern
329 US, coincide with the contingency category B. These differences are expected and can be
330 interpreted as follows: when the WRF model misses clouds (clear sky in the CNTR simulation,
331 category C) or underestimates COD (as seen in Fig. 2), surface O₃ is overestimated. When the
332 WRF model generates clouds that are not present in reality (clear sky in the satellite retrievals,
333 category B), surface O₃ is underestimated. It should be noted that not all regions belonging to

334 category B or C have significant O₃ differences. Interestingly, the regions exhibiting significantly
335 large O₃ differences coincide with large urban areas, e.g., Seattle, WA; Los Angeles, CA;
336 Chicago, IL; Cleveland, OH; Houston, TX; New Orleans, LA; Atlanta, GA; and Miami, FL. The
337 reasons for this result are explored in section 5.4 and 5.5.

338 The performance of the GOES simulation is found to be better than that of the CNTR simulation
339 as compared to observations: for example, under cloudy conditions (COD > 20, see section 5.4
340 for the criterion), the root-mean-square error of MDA8 O₃ in the GOES (CNTR) simulation is
341 13.2 ppb (16.9 ppb) and the correlation coefficient of MDA8 O₃ in the GOES (CNTR)
342 simulation is 0.5 (0.4).

343 **5.3. Relative contribution to O₃ errors from photolysis rates and BVOC emissions**

344 It is expected that reduced BVOC emissions (especially isoprene) due to the presence of clouds
345 can also decrease O₃ formation. Figure 6 shows the spatial distributions of relative changes in
346 PAR and isoprene emission between the EMIS_BVOC and GOES simulations averaged over a
347 10-day period. Because the WRF model tends to underestimate COD or is not able to reproduce
348 clouds in Midwestern and western US, PAR and biogenic isoprene emissions are larger in the
349 EMIS_BVOC simulation than in the GOES simulation. On the other hand, the model
350 overestimates COD or produces clouds that are not present in reality over the southeast US, so
351 PAR and biogenic isoprene emissions are lower in the EMIS_BVOC simulation than in the
352 GOES simulation. The change in PAR (biogenic isoprene emissions) resulting from the
353 difference in clouds fields between the WRF model and satellite retrievals is up to ±30–40%
354 (±25%). Figure 6d shows the relative O₃ difference between EMIS_BVOC and GOES
355 simulations to O₃ difference between CNTR and GOES simulations (Fig. 6c). It is seen that the
356 contribution of changes in BVOC emissions is considerable only for some regions and it ranges

357 from ~10–40%. The average contribution of changes in BVOC emissions over land is ~20%
358 compared to changes of BVOC emissions plus photolysis rates using GOES satellite clouds. The
359 contribution of BVOC emissions is larger (~40%) in urban areas over the southeast (specifically
360 in Charlotte, NC). The difference in O₃ in Charlotte, NC resulting from changes in BVOC
361 emissions is about 1.5 ppb and that from changes in both photolysis rates and BVOC emissions
362 is about 3.5 ppb. In some regions, such as Midwestern, western Pennsylvania, and central New
363 York, the effect of BVOC emissions is negligible.

364

365 **5.4. Cloud effects on ozone bias in VOC- and NO_x-limited regimes**

366 In this section, we examine the effects of clouds on O₃ in VOC-limited and NO_x-limited regimes
367 in order to understand the reasons for a stronger O₃ response to cloud corrections in urban areas
368 than in the remote regions. Figure 7 shows how cloud corrections affect O₃ errors in different
369 regimes. Here, MDA8 O₃ is used to compute the model O₃ bias (simulation minus observation).
370 Figures 7a and 7b show the probability density functions of the model O₃ bias for the CNTR and
371 GOES simulations, respectively, at all ground sites experiencing considerably thick (COD > 20)
372 clouds. In this example, an EPA site is considered under cloudy sky conditions when hourly
373 COD greater than the chosen threshold (here, 20) is present at the site for at least 4 hours within
374 the 8-h time window in a given day. The decrease in the O₃ bias for VOC-limited regime is
375 significant, and the difference in median values between the two simulations is 5.2 ppb. The
376 decrease in O₃ bias for NO_x-limited regimes (2.7 ppb) is about 2 times smaller than that for
377 VOC-limited regime. An important result is that the frequency of very large biases (e.g., greater
378 than 20 ppb) is substantially reduced when cloud fields are corrected, especially for the VOC-

379 limited regime. This implies that more accurate cloud predictions ultimately improve the
380 accuracy of O₃ alert predictions, especially in polluted urban areas.

381 Figure 7c shows the change in median values of MDA8 O₃ bias for a range of COD thresholds.
382 We find that the O₃ bias increases with increasing cloudiness in the CNTR simulation. As
383 previously mentioned, the O₃ bias is generally larger for VOC-limited regimes than for NO_x-
384 limited regimes. When the radiation fields are corrected with satellite clouds, the model O₃ bias
385 is considerably reduced (but not zero). In addition, the O₃ bias in the GOES simulation does not
386 increase as much as that in the CNTR simulation when cloudiness increases. This implies that
387 there are other sources of O₃ biases in the GOES simulation, which are not likely associated with
388 cloudiness. The other errors sources can be precursor emissions, mixing/transport, and deposition.
389 Fig. 7d compares the median values of MDA8 O₃ bias between the two simulations (CNTR
390 minus GOES), and shows that the difference in MDA8 O₃ between the two simulations clearly
391 increases as the COD threshold increases and that the effect of cloud correction is larger in VOC-
392 limited than in NO_x-limited regimes. The reduced O₃ bias as a result of cloud corrections ranges
393 from 1 to 5 ppb depending on CODs and chemistry regimes. This represents up to ~40% of the
394 total O₃ bias under cloudy conditions in the current model version (e.g., 5.2 ppb of 12.6 ppb for
395 COD threshold of 20 in VOC-limited regimes). Note that the results for the sites in transitional
396 zone (the slope of $\Delta O_3/\Delta NO_y$ is 4–6) showed that the effects of cloud in the transitional zone are
397 intermediate; that is, larger than those for NO_x-limited regimes but smaller than those for VOC-
398 limited regimes (not shown).

399 We performed additional analysis by dividing VOC- and NO_x-limited sites into groups that have
400 similar ranges of peak MDA8 O₃ concentration during the period of June–September 2013 (Fig.
401 S3). All sites are grouped into bins with peak value of MDA8 O₃ ranging from larger than 75

402 ppb, 70–75 ppb, 65–70 ppb, 60–65 ppb, to smaller than 60 ppb. The maximum reduction in O₃
403 bias due to cloud corrections is obtained for the VOC-limited sites with peak MDA8 O₃ of 65–70
404 ppb and reaches ~8 ppb. The maximum reduction for NO_x-limited sites, on the other hand, is ~4
405 ppb and found for the sites with peak MDA8 O₃ of 70–75 ppb. Although the degree of the O₃
406 bias reduction varies somewhat among the bins for a given ozone regime, the effects of cloud
407 correction on O₃ bias reduction remain larger in VOC-limited regimes than NO_x-limited regimes.

408 We examine the O₃ bias over the southeast US where large overpredictions at the surface have
409 been reported (e.g., Travis et al. 2016) in the supplementary material. It is found that a
410 considerable portion of O₃ bias is attributable to inaccurate cloud predictions over the southeast
411 US, but the degree of the effects of clouds is smaller than that over CONUS as a whole (Fig. S4).
412 The maximum reduction in O₃ bias due to inaccurate cloud predictions is 4.5 ppb over the
413 southeast US and 5.3 ppb over CONUS. Still, large O₃ biases of ~11 ppb are present over the
414 southeast US (compared to those of 6–9 ppb over CONUS) even though the clouds and radiation
415 fields that are relevant to photochemistry are corrected. This result implies that errors resulting
416 from other processes exist and are responsible for the surface O₃ overpredictions over the
417 southeast US. More in-depth studies that find and quantify errors are therefore required to better
418 predict the O₃ over the southeast US as well as CONUS.

419

420 **5.5. Ozone formation sensitivity to changes in photolysis rates**

421 The difference in O₃ sensitivity to changes in photolysis rates (resulting from the presence of
422 clouds) in different regimes is determined by calculating $d\ln(\text{O}_3)/d\ln(\text{JNO}_2)$ ratios as in
423 Kleinman (1991). Table 3 lists those sensitivity coefficients of O₃ to JNO₂ and shows that O₃ is

424 more sensitive to JNO_2 in VOC-limited than in NO_x -limited regimes, being 1.69 times larger
425 under cloudy-sky conditions and by 1.65 times greater under clear-sky conditions. Similar
426 sensitivities were reported for OH by Berresheim et al. (2003) with the sensitivity of OH to JO^1D ,
427 $\text{dln}(\text{OH})/\text{dln}(\text{JO}^1\text{D})$, of 0.8 at high NO_2 levels (~ 10 ppb) and 0.68 at low to moderate NO_2 levels
428 (~ 1 ppb). The corresponding sensitivities from our study are 1.1 for VOC-limited regimes and
429 0.66 for NO_x -limited regimes under clear-sky conditions. Similar results are also found for the
430 net chemical production of O_3 and OH concentration, revealing stronger responses to changes in
431 cloudiness in VOC-limited regimes than NO_x -limited regimes (Fig. 8). It is interesting to note
432 that OH and HO_2 have local maxima at CODs between 2 and 5. As shown in Ryu et al. (2017),
433 the enhancement of actinic flux at the surface due to optically thin clouds (CODs < 5) is
434 considerable for high-level clouds, i.e., cirrus. The local maxima, therefore, likely result from the
435 fact that the GOES clouds have the largest portion of cirrus for CODs of 2–5 as seen in Fig. 2b.
436 Figure 8 also shows that the variation (defined by 25 and 75 percentiles) of net chemical
437 production of O_3 with respect to COD is much larger in VOC-limited conditions. This result
438 suggests that predicting O_3 under cloudy conditions is likely more difficult in VOC-limited than
439 in NO_x -limited regimes. It is also noticeable that the HO_2 radical concentration remains
440 relatively high in NO_x -limited regimes even under cloudy conditions as compared to the VOC-
441 limited regimes. Note that the results of WRF-Chem here include the effects of both photolysis
442 rates and BVOC emissions.

443 A simplified box model (BOXMOX, Knote et al. (2015)) simulation using the same chemical
444 mechanism (MOZART-4) as WRF-Chem was performed to better understand O_3 sensitivity to
445 changing cloudiness in different chemistry regimes. The emission rates for VOC-limited (NO_x -
446 limited) regime are those of the Chicago urban (rural) area in the WRF-Chem simulation. The

447 initial conditions are taken from the CNTR simulation at 09 CST 7 July 2013 in the Chicago
448 suburban area for both regimes. Dry deposition is not considered. Photolysis rates for all species
449 that are photodissociable are varied from clear-sky to cloudy conditions with up to 80%
450 reduction. The 80% reduction roughly corresponds to COD of 35 (not shown). The box model is
451 integrated for 3 hours and photolysis rates are kept constant during the simulation (i.e., no
452 diurnal variations). The box model results are found to be consistent with the results from the
453 WRF-Chem simulations: the variations of O_3 and OH with respect to decreasing photolysis rates
454 are larger in VOC-limited regime than in NO_x -limited regime (Fig. S5, in the supplementary
455 material). Note that the net chemical production of O_3 obtained from the box model results also
456 shows a larger sensitivity to cloudiness in VOC-limited regimes than in NO_x -limited regimes,
457 which is similar to Figs. 8a and 8d (not shown). Figure 9 shows production and loss terms of
458 $RO_x (= OH + HO_2 + RO_2)$ radicals with variations in photolysis rates for VOC-limited and NO_x -
459 limited regimes. In both regimes, the decreased sunlight due to clouds reduces OH formation by
460 photodissociation of O_3 (primary source of OH). The larger sensitivity of OH radicals to COD in
461 VOC-limited regimes as seen in Fig. 8 is associated with the loss of OH by the radical
462 termination reaction between OH and NO_2 under NO_x -rich conditions, which leads to the large
463 decrease in OH (Fig. 9a). On the other hand, in NO_x -limited regimes, the radical termination
464 reactions are the radical-radical reactions (Fig. 9b). In this regime, OH mainly reacts with VOCs
465 and propagates through radical cycles by producing HO_2/RO_2 radicals, rather than being
466 terminated by the reaction with NO_2 . Given that the reaction between NO and HO_2 becomes the
467 largest source of OH budget (secondary source of OH) at an NO_x concentration of ~ 1 ppb
468 (Ehhalt and Rohrer, 2000; Eisele et al., 1997), OH can be relatively less sensitive to the changes
469 in radiation. Note that the mean daytime NO_x concentration over CONUS in NO_x -limited

470 regimes is 1.2 ppb and that in VOC-limited regimes is 6.7 ppb for this study period. Another
471 attribute is a greater contribution of H₂O₂ photodissociation to the production of RO_x in NO_x-
472 limited regimes than that of HNO₃, which is negligible. Unlike the radical terminated in VOC-
473 limited conditions, a non-negligible amount of terminated radicals can be recycled in the NO_x-
474 limited regime.

475

476 **6. Sensitivity of cloud optical depth and O₃ to microphysics and** 477 **convective schemes**

478 It should be emphasized that our study was performed using a specific representation of the
479 cloud microphysics by Morrison et al. (2009) and cumulus parameterization (Grell and Devenyi,
480 2002). To test the robustness of our results with regard to the representation of clouds, another
481 microphysics scheme, Thompson scheme (Thompson et al., 2008), is employed for a 10-day (3
482 July–12 July 2013) sensitivity simulation. The COD comparison in Fig. S6 shows that with the
483 Thompson scheme the model predicts fewer clouds for all ranges of CODs as compared to
484 GOES retrievals, except for the very thin ones (COD < 1) in which the number of those clouds is
485 still overpredicted as seen in the simulation with Morrison scheme. Compared to the Morrison
486 scheme, the Thompson scheme produces significantly less high-level (cirrus) clouds. This is also
487 consistent with the findings of Cintineo et al. (2013). Despite this difference, the shape of the
488 COD distribution from the two microphysics schemes are rather similar to each other.

489 The MDA8 O₃ bias with the Thompson scheme is evaluated (Fig. S7), and compared to that of
490 the Morrison scheme for the same period. Under the conditions of COD greater than 20, for
491 example, the baseline simulation with the Thompson scheme (that uses model generated clouds)

492 shows that a median bias (14.79 ppb) is a bit smaller than that with the Morrison scheme (16.22
493 ppb) for that period in VOC-limited regimes. In the sensitivity simulation with the Thompson
494 scheme that uses GOES satellite clouds for photochemistry, the median bias is reduced by 5.45
495 ppb (~37%, Fig. S7a) in VOC-limited regimes and by 2.06 ppb (~20%, Fig. S7c) in NO_x-limited
496 regimes, which are consistent with the results of our base simulation. The degree of the effects of
497 cloud correction in the sensitivity simulations with the Thompson scheme, ranging from 0.5 to
498 5.5 ppb, is similar to that found in our base simulation with the Morrison scheme. Therefore, the
499 general conclusions remain the same: i.e., errors in O₃ predictions resulting from errors in cloud
500 predictions are considerable (up to ~5 ppb on average) and the effects of cloud corrections are
501 larger in VOC-limited regimes than in NO_x-limited regimes.

502 To estimate the sensitivity of our results to cumulus parameterization schemes, sensitivity
503 simulations with the Grell-Freitas scheme (Grell and Freitas, 2014) are performed. As done for
504 microphysics scheme, a period of 10 days (3–12 July 2013) was considered. In Fig. S8, the
505 histograms of cloud optical depths obtained for the 10-day period from Grell-Freitas scheme and
506 from Grell-3D scheme show that the distributions of cloud optical depths are in general similar
507 to each other. The Grell-Freitas scheme tends to produce fewer clouds with small or moderate
508 cloud optical depths (Fig. S8). As shown in Fig. S9, the degree of cloud correction in reducing
509 O₃ bias is larger in VOC-limited regimes than in NO_x-limited regimes in the simulation with
510 Grell-Freitas scheme, and thus the conclusions originally drawn remain unchanged.

511

512 **7. Conclusions and discussion**

513 We performed quantitative analyses of the WRF-Chem model meso-scale (12 km) simulations to
514 determine how much errors in cloud predictions contribute to errors in surface O₃ predictions
515 during summertime over CONUS. Clouds were generated using the Morrison microphysics and
516 Grell 3D cumulus parameterization schemes. It is found that the WRF-Chem model is able to
517 generate roughly 55% of the clouds in the right locations by comparing to satellite clouds. A
518 quantitative comparison of COD shows that the WRF-Chem model predicts too many thin cirrus
519 clouds with CODs less than 1, and also considerably underpredicts the optical depths for a
520 majority of cloud systems.

521 The errors in cloud predictions can lead to large hourly O₃ biases of up to 60 ppb, for example,
522 for specific cases in which the model misses deep convective clouds that are present in reality.
523 On average, the errors in MDA8 O₃ of 1–5 ppb are found to be attributable to errors in cloud
524 predictions under cloudy sky conditions. We quantify separately the contribution of changes in
525 photolysis rates and emissions of light-dependent BVOCs to cloud-related errors in surface O₃.
526 The contribution of photolysis rates to surface O₃ is larger (~80% on average) than that of BVOC
527 emissions. The contribution of BVOC emissions to O₃ can become important (~40%) in the
528 VOC-limited regimes where BVOC emissions are large (i.e., cities of the southeast US).

529 The effects of cloud corrections are more impactful in VOC-limited (or high-NO_x) than in NO_x-
530 limited (or low-NO_x) regimes. The sensitivity of O₃ with respect to COD is about 2 times larger
531 in VOC-limited than in NO_x-limited regimes. This finding is consistent with the box modeling
532 results that were performed for typical urban/rural conditions under varying photolysis rates. The
533 production of radicals (OH, HO₂, and RO₂) decreases with decreasing photolysis rates in the
534 presence of clouds. The primary reason for the larger sensitivity of O₃ formation to clouds in

535 VOC-limited regimes is that the loss of OH is much stronger in VOC-limited regimes due to the
536 reaction with NO₂. Thus, OH cannot readily propagate through the radical cycles. In NO_x-
537 limited regimes, the radicals terminated from the radical cycles are mostly HO₂ and RO₂ rather
538 than OH. Thus, OH can remain in the cycles and continue to produce HO₂ and RO₂ by reacting
539 with VOCs before termination. The interconversion of HO₂ to OH is the dominant process in
540 NO_x-limited regimes, and therefore OH and O₃ formations are less sensitive to changes in
541 radiation.

542 We showed that considerable reduction in O₃ bias is achieved by correcting cloud-related
543 radiation fields; however, O₃ is still overpredicted by the WRF-Chem model. The remaining bias
544 likely results from other processes involved in the O₃ lifecycle such as precursor emissions from
545 both anthropogenic and biogenic sources, transport, turbulent mixing, and dry deposition, which
546 quantitative assessment is beyond the scope of this study.

547 One should keep in mind that the quantitative estimate of the O₃ bias related to the cloud effects
548 on radiation as reported in this study could be sensitive to several factors. In particular, this study
549 is based on a particular configuration of the WRF-Chem model with regard to the radiation,
550 microphysics, cumulus, boundary layer parameterization and the chemistry scheme. We have
551 tested the sensitivity of our results to the choice of microphysics and cumulus parameterization
552 schemes, and have shown that MDA8 O₃ biases are reduced by up to ~5 ppb with the satellite
553 cloud corrections in the simulations with the different microphysics and cumulus
554 parameterization schemes, which is consistent with the results found in our base simulations.

555 This study suggests that accurate cloud predictions through data assimilation or cloud mask
556 corrections with near-real time satellite cloud data would improve the accuracy of O₃ predictions

557 and that the benefit is expected to be greater in VOC-limited than in NO_x-limited regimes. It
558 should be noted that our estimates are based on WRF-Chem simulations that use initial and
559 boundary conditions from meteorological analysis data, which is an improved estimate of the
560 meteorological state compared to forecast data, and thus the reduction of errors in O₃ predictions
561 could be even greater in a forecasting setting. From the perspective of O₃ forecast, our study
562 indicates that there is a need for an enhanced understanding of the evolution of errors in O₃
563 forecasts associated with errors in cloud forecasts, and for optimizing the use of meteorological
564 forecasts to allow more accurate near-term O₃ predictions. The present study corrects cloud
565 fields in WRF using satellite clouds only for radiation that is relevant to photochemistry, and
566 those cloud corrections do not affect other meteorological variables such as surface temperature,
567 wind, humidity, boundary layer height, etc. In a future study, we plan to examine the effects of
568 satellite cloud assimilation on near-term O₃ forecasts using enhanced forecasts such as the Rapid
569 Refresh products from NOAA (Benjamin et al., 2016) that take into account cloud data
570 assimilation to derive meteorology. The Rapid Refresh uses satellite cloud products as well as
571 cloud observations from the ground and considers the thermodynamic balance between
572 temperature and humidity due to the presence of clouds. Thus, this will allow investigating the
573 effects of cloud assimilation on O₃ forecasts not only through changes in radiation for
574 photochemistry but also through changes in meteorological variables.

575

576 **Acknowledgments**

577 We acknowledge Samuel Hall and Kirk Ullmann for providing actinic flux data that are used for
578 supplementary analysis, George Grell and Geoff Tyndall for helpful discussions. This study is

579 supported from NASA-ROSES grant NNX15AE38G. P. Minnis was supported by the NASA
580 Modeling, Analysis, and Prediction Program. The National Center for Atmospheric Research is
581 sponsored by the National Science Foundation. We would like to acknowledge high-performance
582 computing support from Cheyenne (doi:10.5065/D6RX99HX) provided by NCAR's
583 Computational and Information Systems Laboratory, sponsored by the National Science
584 Foundation. The GOES cloud retrievals are available at <https://satcorps.larc.nasa.gov>. The EPA
585 ozone data can be downloaded at
586 https://aqedr1.epa.gov/aqsweb/aqstmp/airdata/download_files.html.

587

588

589

590

591

592

593

594

595

596

597

599 **Reference**

600 Bei, N., Lei, W., Zavala, M. and Molina, L. T.: Ozone predictabilities due to meteorological
601 uncertainties in the Mexico City basin using ensemble forecasts, *Atmos Chem Phys*, 10(13),
602 6295–6309, doi:10.5194/acp-10-6295-2010, 2010.

603 Benjamin, S. G., Weygandt, S. S., Brown, J. M., Hu, M., Alexander, C. R., Smirnova, T. G.,
604 Olson, J. B., James, E. P., Dowell, D. C., Grell, G. A., Lin, H., Peckham, S. E., Smith, T. L.,
605 Moninger, W. R., Kenyon, J. S. and Manikin, G. S.: A North American Hourly Assimilation and
606 Model Forecast Cycle: The Rapid Refresh, *Mon. Wea. Rev.*, 144(4), 1669–1694,
607 doi:10.1175/MWR-D-15-0242.1, 2015.

608 Berresheim, H., Plass-Dülmer, C., Elste, T., Mihalopoulos, N. and Rohrer, F.: OH in the coastal
609 boundary layer of Crete during MINOS: Measurements and relationship with ozone photolysis,
610 *Atmos Chem Phys*, 3(3), 639–649, doi:10.5194/acp-3-639-2003, 2003.

611 Briegleb, B. P.: Delta-Eddington approximation for solar radiation in the NCAR community
612 climate model, *J. Geophys. Res. Atmospheres*, 97(D7), 7603–7612, doi:10.1029/92JD00291,
613 1992.

614 Brioude, J., Angevine, W. M., Ahmadov, R., Kim, S.-W., Evan, S., McKeen, S. A., Hsie, E.-Y.,
615 Frost, G. J., Neuman, J. A., Pollack, I. B., Peischl, J., Ryerson, T. B., Holloway, J., Brown, S. S.,
616 Nowak, J. B., Roberts, J. M., Wofsy, S. C., Santoni, G. W., Oda, T. and Trainer, M.: Top-down
617 estimate of surface flux in the Los Angeles Basin using a mesoscale inverse modeling technique:
618 assessing anthropogenic emissions of CO, NO_x and CO₂ and their impacts, *Atmos Chem Phys*,
619 13(7), 3661–3677, doi:10.5194/acp-13-3661-2013, 2013.

620 Brown-Steiner, B., Hess, P. G. and Lin, M. Y.: On the capabilities and limitations of GCCM
621 simulations of summertime regional air quality: A diagnostic analysis of ozone and temperature
622 simulations in the US using CESM CAM-Chem, *Atmos. Environ.*, 101, 134–148,
623 doi:10.1016/j.atmosenv.2014.11.001, 2015.

624 Campbell, P., Zhang, Y., Yahya, K., Wang, K., Hogrefe, C., Pouliot, G., Knote, C., Hodzic, A.,
625 San Jose, R., Perez, J. L., Jimenez Guerrero, P., Baro, R. and Makar, P.: A multi-model
626 assessment for the 2006 and 2010 simulations under the Air Quality Model Evaluation
627 International Initiative (AQMEII) phase 2 over North America: Part I. Indicators of the
628 sensitivity of O₃ and PM_{2.5} formation regimes, *Atmos. Environ.*, 115, 569–586,
629 doi:10.1016/j.atmosenv.2014.12.026, 2015.

630 Carter, W. P. L.: Development of the SAPRC-07 chemical mechanism, *Atmos. Environ.*, 44(40),
631 5324–5335, doi:10.1016/j.atmosenv.2010.01.026, 2010.

632 Chang, J. S., Brost, R. A., Isaksen, I. S. A., Madronich, S., Middleton, P., Stockwell, W. R. and
633 Walcek, C. J.: A three-dimensional Eulerian acid deposition model: Physical concepts and
634 formulation, *J. Geophys. Res. Atmospheres*, 92(D12), 14681–14700,
635 doi:10.1029/JD092iD12p14681, 1987.

636 Chen, F. and Dudhia, J.: Coupling an Advanced Land Surface–Hydrology Model with the Penn
637 State–NCAR MM5 Modeling System. Part I: Model Implementation and Sensitivity, *Mon.*
638 *Weather Rev.*, 129(4), 569–585, doi:10.1175/1520-0493(2001)129<0569:CAALSH>2.0.CO;2,
639 2001.

640 Cintineo, R., Otkin, J. A., Xue, M. and Kong, F.: Evaluating the Performance of Planetary
641 Boundary Layer and Cloud Microphysical Parameterization Schemes in Convection-Permitting
642 Ensemble Forecasts Using Synthetic GOES-13 Satellite Observations, *Mon. Weather Rev.*,
643 142(1), 163–182, doi:10.1175/MWR-D-13-00143.1, 2013.

644 Cleary, P. A., Fuhrman, N., Schulz, L., Schafer, J., Fillingham, J., Bootsma, H., McQueen, J.,
645 Tang, Y., Langel, T., McKeen, S., Williams, E. J., and Brown, S. S.: Ozone distributions over
646 southern Lake Michigan: comparisons between ferry-based observations, shoreline-based DOAS
647 observations and model forecasts, *Atmos. Chem. Phys.*, 15, 5109-5122,
648 <https://doi.org/10.5194/acp-15-5109-2015>, 2015.

649 Dabberdt, W. F., Carroll, M. A., Baumgardner, D., Carmichael, G., Cohen, R., Dye, T., Ellis, J.,
650 Grell, G., Grimmond, S., Hanna, S., Irwin, J., Lamb, B., Madronich, S., McQueen, J., Meagher,
651 J., Odman, T., Pleim, J., Schmid, H. P. and Westphal, D. L.: Meteorological Research Needs for
652 Improved Air Quality Forecasting: Report of the 11th Prospectus Development Team of the U.S.
653 Weather Research Program*, *Bull. Am. Meteorol. Soc.*, 85(4), 563–586, doi:10.1175/BAMS-85-
654 4-563, 2004.

655 Ehhalt, D. H. and Rohrer, F.: Dependence of the OH concentration on solar UV, *J. Geophys. Res.*
656 *Atmospheres*, 105(D3), 3565–3571, doi:10.1029/1999JD901070, 2000.

657 Eisele, F. L., Mount, G. H., Tanner, D., Jefferson, A., Shetter, R., Harder, J. W. and Williams, E.
658 J.: Understanding the production and interconversion of the hydroxyl radical during the
659 Tropospheric OH Photochemistry Experiment, *J. Geophys. Res. Atmospheres*, 102(D5), 6457–
660 6465, doi:10.1029/96JD02207, 1997.

661 Fiore, A. M., Dentener, F. J., Wild, O., Cuvelier, C., Schultz, M. G., Hess, P., Textor, C., Schulz,
662 M., Doherty, R. M., Horowitz, L. W., MacKenzie, I. A., Sanderson, M. G., Shindell, D. T.,
663 Stevenson, D. S., Szopa, S., Van Dingenen, R., Zeng, G., Atherton, C., Bergmann, D., Bey, I.,
664 Carmichael, G., Collins, W. J., Duncan, B. N., Faluvegi, G., Folberth, G., Gauss, M., Gong, S.,
665 Hauglustaine, D., Holloway, T., Isaksen, I. S. A., Jacob, D. J., Jonson, J. E., Kaminski, J. W.,
666 Keating, T. J., Lupu, A., Marmer, E., Montanaro, V., Park, R. J., Pitari, G., Pringle, K. J., Pyle, J.
667 A., Schroeder, S., Vivanco, M. G., Wind, P., Wojcik, G., Wu, S. and Zuber, A.: Multimodel
668 estimates of intercontinental source-receptor relationships for ozone pollution, *J. Geophys. Res.*
669 *Atmospheres*, 114(D4), D04301, doi:10.1029/2008JD010816, 2009.

670 Grell, G. A. and Devenyi, D.: A generalized approach to parameterizing convection combining
671 ensemble and data assimilation techniques, *Geophys. Res. Lett.*, 29(14), 38–1,
672 doi:10.1029/2002GL015311, 2002.

673 Grell, G. A. and Freitas, S. R.: A scale and aerosol aware stochastic convective parameterization
674 for weather and air quality modeling, *Atmos. Chem. Phys.*, 14, 5233–5250,
675 <https://doi.org/10.5194/acp-14-5233-2014>, 2014.

676 Guenther, A., Karl, T., Harley, P., Wiedinmyer, C., Palmer, P. I. and Geron, C.: Estimates of
677 global terrestrial isoprene emissions using MEGAN (Model of Emissions of Gases and Aerosols
678 from Nature), *Atmos Chem Phys*, 6(11), 3181–3210, doi:10.5194/acp-6-3181-2006, 2006.

679 Hodzic, A., Ryu, Y.-H., Madronich, S., Walters, S.: Modeling and evaluation of actinic fluxes
680 and photolysis rates in WRF-Chem, In preparation.

681 Iacono, M. J., Delamere, J. S., Mlawer, E. J., Shephard, M. W., Clough, S. A. and Collins, W. D.:
682 Radiative forcing by long-lived greenhouse gases: Calculations with the AER radiative transfer
683 models, *J. Geophys. Res. Atmospheres*, 113(D13), D13103, doi:10.1029/2008JD009944, 2008.

684 Im, U., Bianconi, R., Solazzo, E., Kioutsioukis, I., Badia, A., Balzarini, A., Baró, R., Bellasio, R.,
685 Brunner, D., Chemel, C., Curci, G., Flemming, J., Forkel, R., Giordano, L., Jiménez-Guerrero, P.,
686 Hirtl, M., Hodzic, A., Honzak, L., Jorba, O., Knote, C., Kuenen, J. J. P., Makar, P. A., Manders-
687 Groot, A., Neal, L., Pérez, J. L., Pirovano, G., Pouliot, G., San Jose, R., Savage, N., Schroder,
688 W., Sokhi, R. S., Syrakov, D., Torian, A., Tuccella, P., Werhahn, J., Wolke, R., Yahya, K.,
689 Zabkar, R., Zhang, Y., Zhang, J., Hogrefe, C. and Galmarini, S.: Evaluation of operational on-
690 line-coupled regional air quality models over Europe and North America in the context of
691 AQMEII phase 2. Part I: Ozone, *Atmos. Environ.*, 115, 404–420,
692 doi:10.1016/j.atmosenv.2014.09.042, 2015.

693 Kleinman, L. I.: Seasonal dependence of boundary layer peroxide concentration: The low and
694 high NO_x regimes, *J. Geophys. Res. Atmospheres*, 96(D11), 20721–20733,
695 doi:10.1029/91JD02040, 1991.

696 Knote, C., Hodzic, A., Jimenez, J. L., Volkamer, R., Orlando, J. J., Baidar, S., Brioude, J., Fast,
697 J., Gentner, D. R., Goldstein, A. H., Hayes, P. L., Knighton, W. B., Oetjen, H., Setyan, A., Stark,
698 H., Thalman, R., Tyndall, G., Washenfelder, R., Waxman, E. and Zhang, Q.: Simulation of semi-
699 explicit mechanisms of SOA formation from glyoxal in aerosol in a 3-D model, *Atmos Chem*
700 *Phys*, 14(12), 6213–6239, doi:10.5194/acp-14-6213-2014, 2014.

701 Knote, C., Tuccella, P., Curci, G., Emmons, L., Orlando, J. J., Madronich, S., Baró, R., Jiménez-
702 Guerrero, P., Luecken, D., Hogrefe, C., Forkel, R., Werhahn, J., Hirtl, M., Pérez, J. L., San José,

703 R., Giordano, L., Brunner, D., Yahya, K. and Zhang, Y.: Influence of the choice of gas-phase
704 mechanism on predictions of key gaseous pollutants during the AQMEII phase-2
705 intercomparison, *Atmos. Environ.*, 115, 553–568, doi:10.1016/j.atmosenv.2014.11.066, 2015.

706 Lin, M., Horowitz, L. W., Payton, R., Fiore, A. M. and Tonnesen, G.: US surface ozone trends
707 and extremes from 1980 to 2014: quantifying the roles of rising Asian emissions, domestic
708 controls, wildfires, and climate, *Atmos Chem Phys*, 17(4), 2943–2970, doi:10.5194/acp-17-
709 2943-2017, 2017.

710 Mayer, B., Fischer, C. A. and Madronich, S.: Estimation of surface actinic flux from satellite
711 (TOMS) ozone and cloud reflectivity measurements, *Geophys. Res. Lett.*, 25(23), 4321–4324,
712 doi:10.1029/1998GL900140, 1998.

713 Minnis, P., Nguyen, L., Palikonda, R., Heck, P. W. Spangenberg, D. A., Doelling, D. R., Ayers,
714 J. K., Smith, W. L., Jr., Khaiyer, M. M., Trepte, Q. Z., Avey, L. A., Chang, F.-L., Yost, C. R.,
715 Chee, T. L., and Sun-Mack, S.: Near-real time cloud retrievals from operational and research
716 meteorological satellites, *Proc. SPIE Remote Sens. Clouds Atmos. XIII*, 7107-2, 8 pp., ISBN:
717 9780819473387, 2008.

718 Minnis, P., Sun-Mack, S., Trepte, Q. Z., Chang, F.-L., Heck, P. W., Chen, Y., Yi, Y., Arduini, R.
719 F., Ayers, K., Bedka, K., Bedka, S., Brown, R., Gibson, S., Heckert, E., Hong, G., Jin, Z.
720 Palikonda, R. Smith, R. Smith, W. l., Jr., Spangenberg, D. A. Yang, P., Yost, C. R., and Xie,
721 Y.: CERES Edition 3 cloud retrievals. *AMS 13th Conf. Atmos. Rad.*, Portland, OR, June 27 – July
722 2, 5.4, 7 pp., 2010.

723 Minnis, P., Sun-Mack, S., Young, D. F., Heck, P. W., Garber, D. P., Chen, Y., Spangenberg, D.
724 A., Arduini, R. F., Trepte, Q. Z., Smith, W. L., Ayers, J. K., Gibson, S. C., Miller, W. F., Hong,

725 G., Chakrapani, V., Takano, Y., Liou, K. N., Xie, Y. and Yang, P.: CERES Edition-2 Cloud
726 Property Retrievals Using TRMM VIRS and Terra and Aqua MODIS Data #x2014;Part I:
727 Algorithms, IEEE Trans. Geosci. Remote Sens., 49(11), 4374–4400,
728 doi:10.1109/TGRS.2011.2144601, 2011.

729 Minnis, P., Bedka, K., Q. Trepte, Q., Yost, C. R., Bedka, S. T., Scarino, B., Khlopenkov, K., and
730 Khaiyer, M. M., 2016: A consistent long-term cloud and clear-sky radiation property dataset
731 from the Advanced Very High Resolution Radiometer (AVHRR), Climate Algorithm
732 Theoretical Basis Document (C-ATBD), CDRP-ATBD-0826 Rev 1 AVHRR Cloud Properties -
733 NASA, NOAA CDR Program, 19 September, 159 pp.,DOI:10.789/V5HT2M8T, 2016.

734 Morrison, H., Thompson, G. and Tatarskii, V.: Impact of Cloud Microphysics on the
735 Development of Trailing Stratiform Precipitation in a Simulated Squall Line: Comparison of
736 One- and Two-Moment Schemes, Mon. Weather Rev., 137(3), 991–1007,
737 doi:10.1175/2008MWR2556.1, 2009.

738 Nakanishi, M. and Niino, H.: An Improved Mellor–Yamada Level-3 Model: Its Numerical
739 Stability and Application to a Regional Prediction of Advection Fog, Bound.-Layer Meteorol.,
740 119(2), 397–407, doi:10.1007/s10546-005-9030-8, 2006.

741 Pour-Biazar, A., McNider, R. T., Roselle, S. J., Suggs, R., Jedlovec, G., Byun, D. W., Kim, S.,
742 Lin, C. J., Ho, T. C., Haines, S., Dornblaser, B. and Cameron, R.: Correcting photolysis rates on
743 the basis of satellite observed clouds, J. Geophys. Res. Atmospheres, 112(D10), D10302,
744 doi:10.1029/2006JD007422, 2007.

745 Rossow, W. B. and Schiffer, R. A.: Advances in Understanding Clouds from ISCCP, Bull. Am.
746 Meteorol. Soc., 80(11), 2261–2287, doi:10.1175/1520-0477(1999)080<2261:AIUCFI>2.0.CO;2,
747 1999.

748 Ryu, Y.-H., Hodzic, A., Descombes, G., Hall, S., Minnis, P., Spangenberg, D., Ullmann, K. and
749 Madronich, S.: Improved modeling of cloudy-sky actinic flux using satellite cloud retrievals,
750 Geophys. Res. Lett., 44(3), 2016GL071892, doi:10.1002/2016GL071892, 2017.

751 Sarwar, G., Godowitch, J., Henderson, B. H., Fahey, K., Pouliot, G., Hutzell, W. T., Mathur, R.,
752 Kang, D., Goliff, W. S. and Stockwell, W. R.: A comparison of atmospheric composition using
753 the Carbon Bond and Regional Atmospheric Chemistry Mechanisms, Atmos Chem Phys, 13(19),
754 9695–9712, doi:10.5194/acp-13-9695-2013, 2013.

755 Sillman, S. and He, D.: Some theoretical results concerning O₃-NO_x-VOC chemistry and NO_x-
756 VOC indicators, J. Geophys. Res. Atmospheres, 107(D22), 4659, doi:10.1029/2001JD001123,
757 2002.

758 Sun-Mack, S., Minnis, P., Chen, Y., Kato, S., Yi, Y., Gibson, S. C., Heck, P. W. and Winker, D.
759 M.: Regional Apparent Boundary Layer Lapse Rates Determined from CALIPSO and MODIS
760 Data for Cloud-Height Determination, J. Appl. Meteorol. Climatol., 53(4), 990–1011,
761 doi:10.1175/JAMC-D-13-081.1, 2014.

762 Tang, W., Cohan, D. S., Pour-Biazar, A., Lamsal, L. N., White, A. T., Xiao, X., Zhou, W.,
763 Henderson, B. H. and Lash, B. F.: Influence of satellite-derived photolysis rates and NO_x
764 emissions on Texas ozone modeling, Atmos Chem Phys, 15(4), 1601–1619, doi:10.5194/acp-15-
765 1601-2015, 2015.

766 Tang, Y., Lee, P., Tsidulko, M., Huang, H.-C., McQueen, J. T., DiMego, G. J., Emmons, L. K.,
767 Pierce, R. B., Thompson, A. M., Lin, H.-M., Kang, D., Tong, D., Yu, S., Mathur, R., Pleim, J. E.,
768 Otte, T. L., Pouliot, G., Young, J. O., Schere, K. L., Davidson, P. M. and Stajner, I.: The impact
769 of chemical lateral boundary conditions on CMAQ predictions of tropospheric ozone over the
770 continental United States, *Environ. Fluid Mech.*, 9(1), 43–58, doi:10.1007/s10652-008-9092-5,
771 2009.

772 Thiel, S., Ammannato, L., Bais, A., Bandy, B., Blumthaler, M., Bohn, B., Engelsen, O., Gobbi,
773 G. P., Gröbner, J., Jäkel, E., Junkermann, W., Kazadzis, S., Kift, R., Kjeldstad, B., Kouremeti, N.,
774 Kylling, A., Mayer, B., Monks, P. S., Reeves, C. E., Schallhart, B., Scheirer, R., Schmidt, S.,
775 Schmitt, R., Schreder, J., Silbernagl, R., Topaloglou, C., Thorseth, T. M., Webb, A. R.,
776 Wendisch, M. and Werle, P.: Influence of clouds on the spectral actinic flux density in the lower
777 troposphere (INSPECTRO): overview of the field campaigns, *Atmos Chem Phys*, 8(6), 1789–
778 1812, doi:10.5194/acp-8-1789-2008, 2008.

779 Thompson, G., Field, P. R., Rasmussen, R. M. and Hall, W. D.: Explicit Forecasts of Winter
780 Precipitation Using an Improved Bulk Microphysics Scheme. Part II: Implementation of a New
781 Snow Parameterization, *Mon. Weather Rev.*, 136(12), 5095–5115,
782 doi:10.1175/2008MWR2387.1, 2008.

783 Toon, O. B., Maring, H., Dibb, J., Ferrare, R., Jacob, D. J., Jensen, E. J., Luo, Z. J., Mace, G. G.,
784 Pan, L. L., Pfister, L., Rosenlof, K. H., Redemann, J., Reid, J. S., Singh, H. B., Thompson, A. M.,
785 Yokelson, R., Minnis, P., Chen, G., Jucks, K. W. and Pszenny, A.: Planning, implementation,
786 and scientific goals of the Studies of Emissions and Atmospheric Composition, Clouds and

787 Climate Coupling by Regional Surveys (SEAC4RS) field mission, *J. Geophys. Res.*
788 *Atmospheres*, 121(9), 2015JD024297, doi:10.1002/2015JD024297, 2016.

789 Travis, K. R., Jacob, D. J., Fisher, J. A., Kim, P. S., Marais, E. A., Zhu, L., Yu, K., Miller, C. C.,
790 Yantosca, R. M., Sulprizio, M. P., Thompson, A. M., Wennberg, P. O., Crouse, J. D., St. Clair,
791 J. M., Cohen, R. C., Laughner, J. L., Dibb, J. E., Hall, S. R., Ullmann, K., Wolfe, G. M., Pollack,
792 I. B., Peischl, J., Neuman, J. A. and Zhou, X.: Why do models overestimate surface ozone in the
793 Southeast United States?, *Atmos Chem Phys*, 16(21), 13561–13577, doi:10.5194/acp-16-13561-
794 2016, 2016.

795 Wiedinmyer, C., Akagi, S. K., Yokelson, R. J., Emmons, L. K., Al-Saadi, J. A., Orlando, J. J.
796 and Soja, A. J.: The Fire INventory from NCAR (FINN): a high resolution global model to
797 estimate the emissions from open burning, *Geosci Model Dev*, 4(3), 625–641, doi:10.5194/gmd-
798 4-625-2011, 2011.

799 Yang, P., Hong, G., Kattawar, G. W., Minnis, P. and Hu, Y.: Uncertainties Associated With the
800 Surface Texture of Ice Particles in Satellite-Based Retrieval of Cirrus Clouds: Part II
801 #x2014;Effect of Particle Surface Roughness on Retrieved Cloud Optical Thickness and
802 Effective Particle Size, *IEEE Trans. Geosci. Remote Sens.*, 46(7), 1948–1957,
803 doi:10.1109/TGRS.2008.916472, 2008.

804 Zhang, F., Bei, N., Nielsen-Gammon, J. W., Li, G., Zhang, R., Stuart, A. and Aksoy, A.: Impacts
805 of meteorological uncertainties on ozone pollution predictability estimated through
806 meteorological and photochemical ensemble forecasts, *J. Geophys. Res. Atmospheres*, 112(D4),
807 D04304, doi:10.1029/2006JD007429, 2007.

808 Zhang, Y., Bocquet, M., Mallet, V., Seigneur, C. and Baklanov, A.: Real-time air quality
809 forecasting, part II: State of the science, current research needs, and future prospects, *Atmos.*
810 *Environ.*, 60, 656–676, doi:10.1016/j.atmosenv.2012.02.041, 2012.

811

812

813

814

815

816

817

818

819

820

821

822

823

824

825

826

827

828

829

830

831 Table 1. Description of WRF-Chem simulations.

	Photolysis rates	PAR	Analysis Period
CNTR	WRF clouds	WRF clouds	06 UTC 11 June–12 UTC 1 October
GOES	GOES clouds	GOES clouds	06 UTC 11 June–12 UTC 1 October
EMIS_BVOC	GOES clouds	WRF clouds	06 UTC 3 July–12 UTC 13 July

832

833

834

835

836

837

838

839

840

841

842

843

844

845

846 Table 2. Contingency table for WRF simulation and GOES satellite clouds. The number of data
 847 for each category is normalized by the total number of data.

		GOES Satellite	
		Cloudy	Clear
WRF simulation	Cloudy	A (hit) 24.8%	B (false alarm) 10.4%
	Clear	C (miss) 19.8%	D (correct negative) 44.9%

848

849

850

851

852

853

854

855

856

857

858

859 Table 3. Sensitivity coefficient of O₃ to JNO₂, i.e., $\text{dln}(\text{O}_3)/\text{dln}(\text{JNO}_2)$. The values of
860 $\text{dln}(\text{O}_3)/\text{dln}(\text{JNO}_2)$ for the period of 09–13 LST are averages over only CONUS EPA stations
861 that have monotonically increasing O₃ concentrations with time.

	Cloudy sky (5 < COD < 20)	Clear sky
VOC-limited	0.59	1.27
NO _x -limited	0.35	0.77

862

863

864

865

866

867

868

869

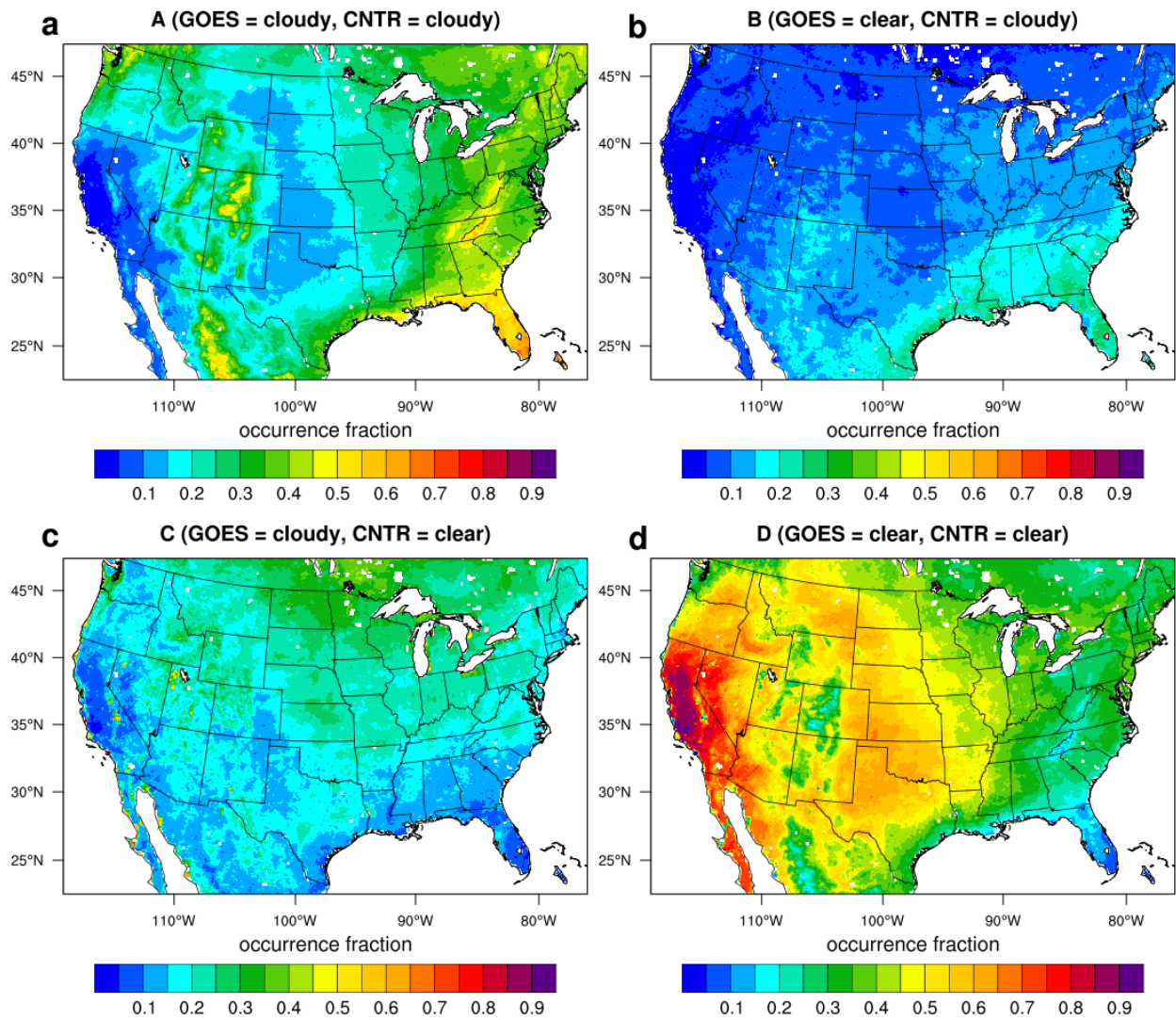
870

871

872

873

874



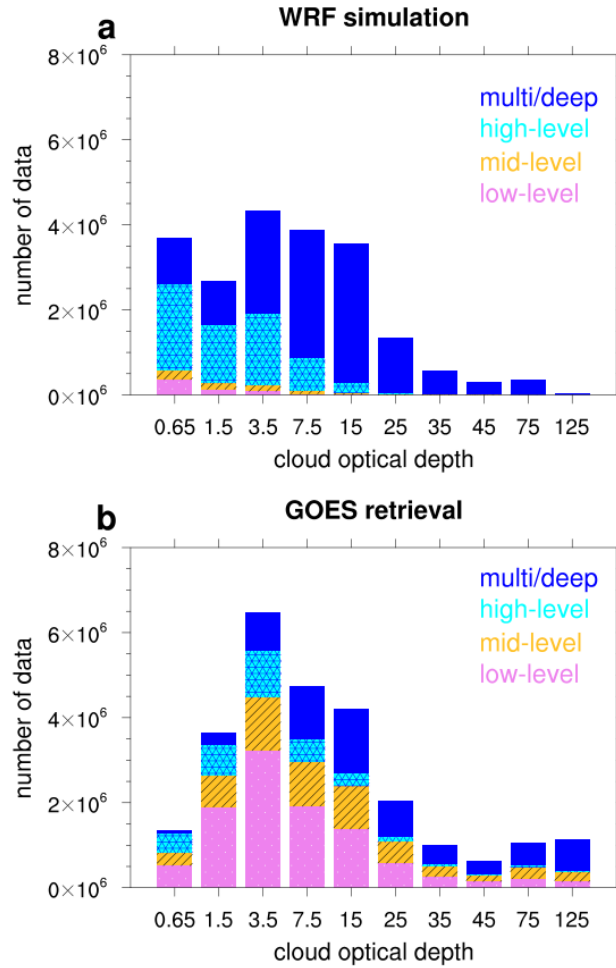
875

876 Fig. 1. Spatial distribution of each contingency category (see Table 2) between the WRF-
 877 generated clouds (CNTR simulation) and SatCORPS GOES retrievals averaged over the whole
 878 study period.

879

880

881

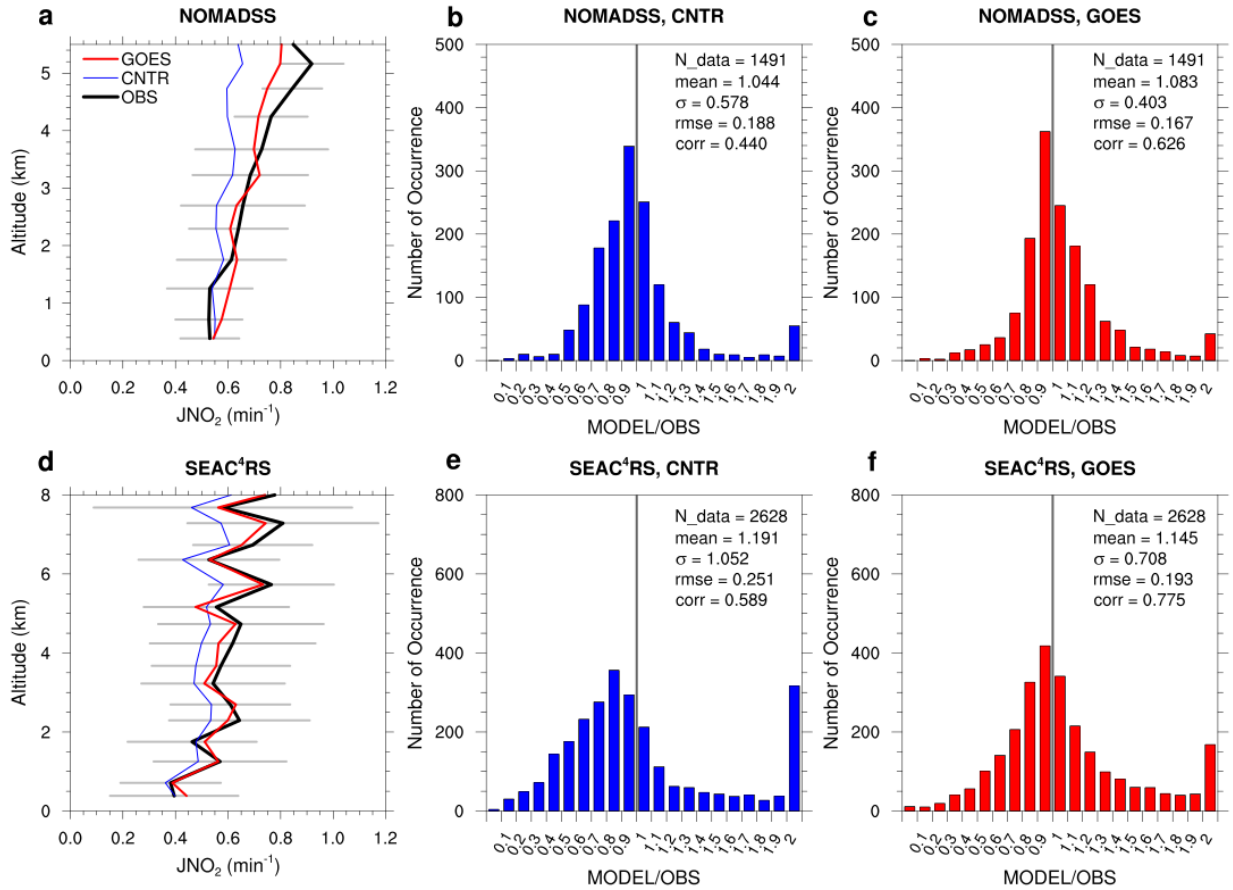


882

883 Fig. 2. Histogram of hourly cloud optical depth (COD) during the daytime (16–23 UTC) over
 884 CONUS (land only) from the (a) WRF simulation (with the Morrison microphysics and the Grell
 885 3-D schemes) and (b) GOES satellite retrievals. CODs on the x -axis represent the mean values of
 886 the bins that are 0.3–1, 1–2, 2–5, 5–10, 10–20, 20–30, 30–40, 40–50, 50–100, and 100–150. For
 887 a fair comparison, the multi-layered WRF clouds are not resolved into cloud layers as this
 888 layering cannot be resolved by the satellite.

889

890

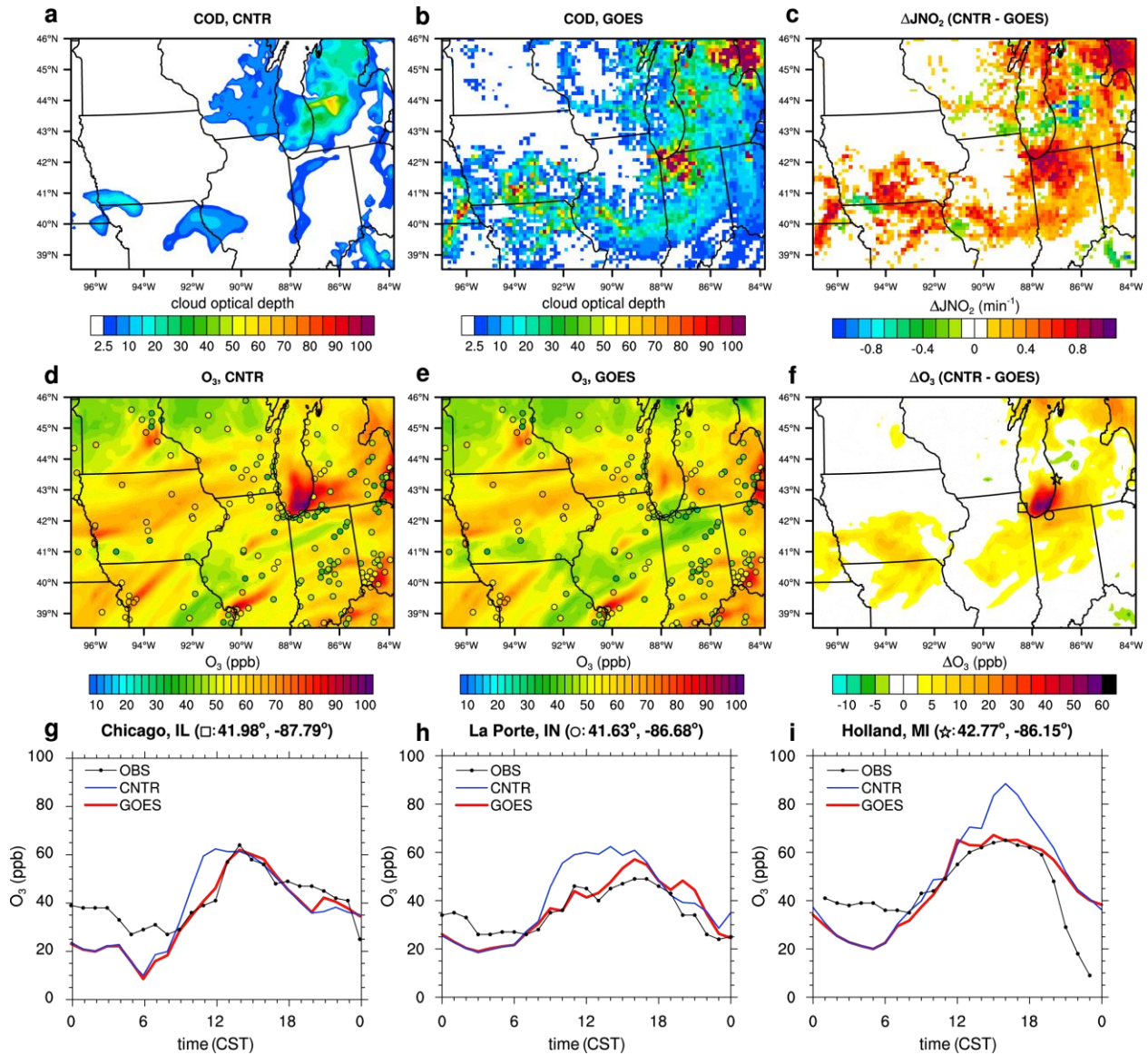


891

892 Fig. 3. Model evaluation with 16 NOMADSS flights (top row) and with 21 SEAC⁴RS flights
 893 (bottom row). Note that only cloudy skies are considered. The comparison is performed for the
 894 averaged vertical profiles of JNO₂ for the (a) NOMADSS and (d) SEAC⁴RS. The gray horizontal
 895 lines indicate the standard deviations from the observations. Histogram of ratio of JNO₂
 896 simulated by the model to JNO₂ observed (b) in the CNTR simulation and (c) in the GOES
 897 simulation for the NOMADSS. (e and f) are the same as (b and c), respectively, but for the
 898 SEAC⁴RS.

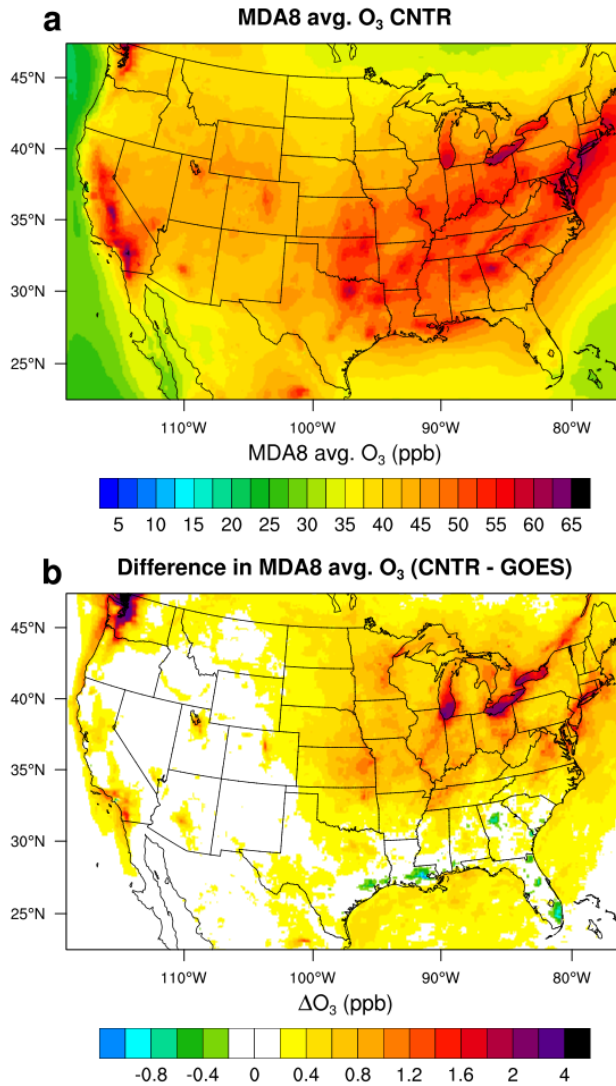
899

900



901

902 Fig. 4. Horizontal distributions of cloud optical depth at 13 CST (= 19 UTC) 8 July 2013 (a) in
 903 the CNTR simulation and (b) in the GOES simulation. Horizontal distributions of O₃ at 13 CST
 904 8 July 2013 at the lowest model level (shaded) (d) in the CNTR simulation and (e) in the GOES
 905 simulation. The circles indicate EPA ozone measurements. (c and f) Difference in JNO₂ and O₃,
 906 respectively, between the simulations (i.e., CNTR simulation minus GOES simulation). (g, h,
 907 and i) Time series of O₃ at the square (Chicago, IL), circle (La Porte, IN), and star (Holland, MI)
 908 that are marked in (f), respectively.



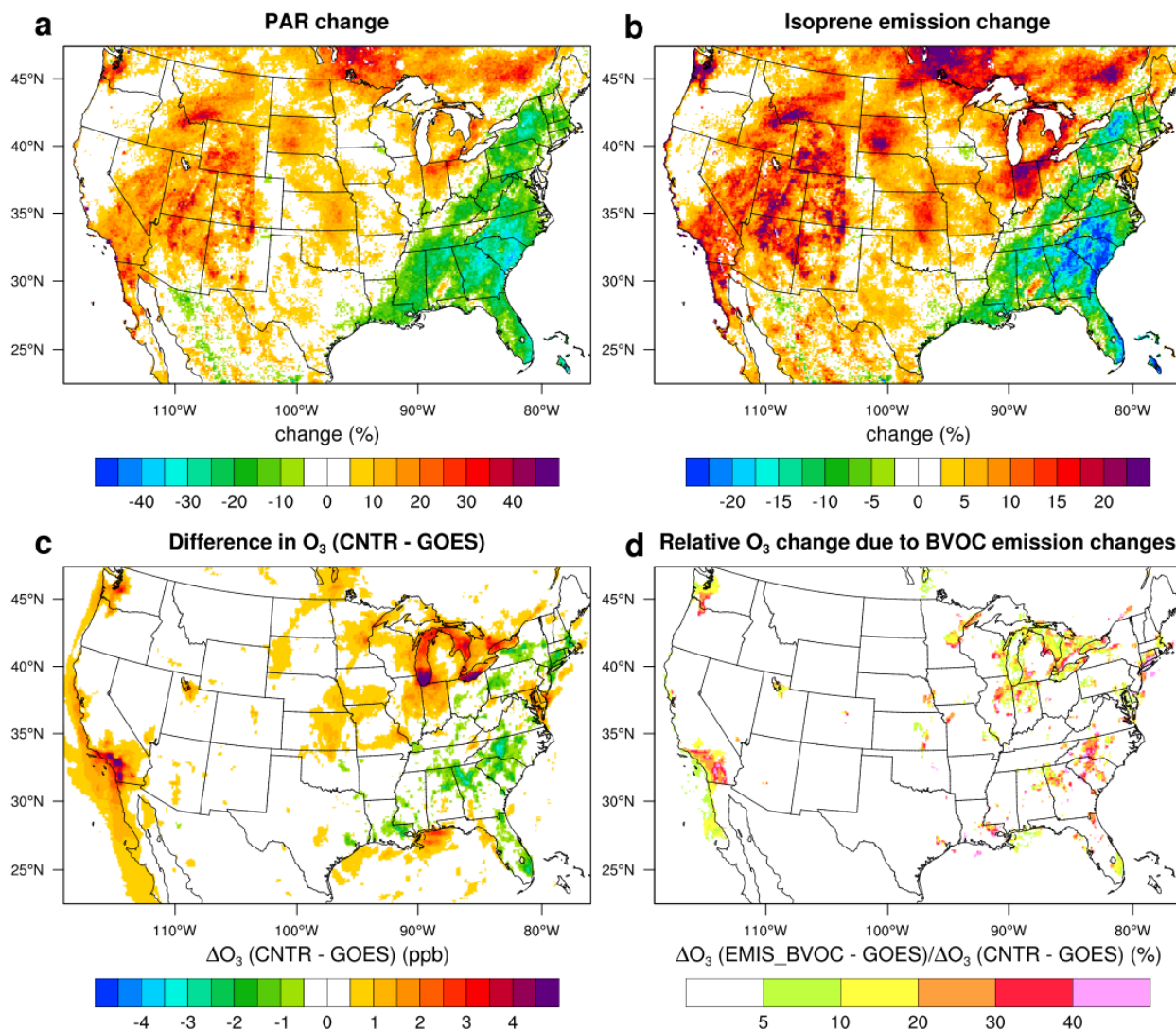
909

910 Fig. 5. (a) Spatial distribution of maximum daily 8-h average O₃ (MDA8 O₃) at the lowest model
 911 level averaged over the whole analysis period in the CNTR simulation. (b) Difference in MDA8
 912 O₃ at the lowest model level between the control and GOES simulations (i.e., CNTR minus
 913 GOES).

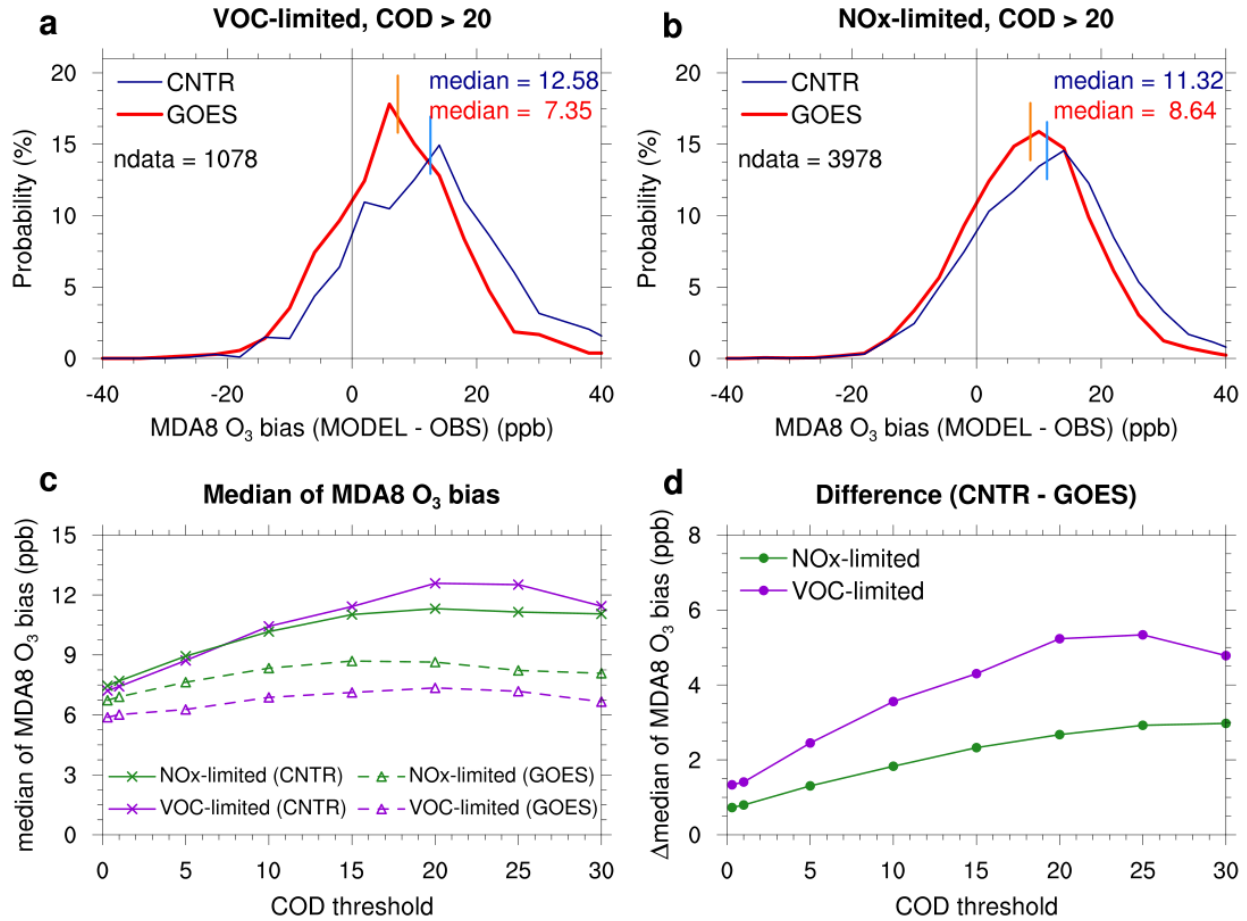
914

915

916



917
 918 Fig. 6. Spatial distributions of (a) PAR change and (b) isoprene emission change from biogenic
 919 sources between EMIS_BVOC and GOES simulations, $(EMIS_BVOC - GOES)/GOES$, averaged
 920 over the period of 3–12 July 2013. (c) Difference in O₃ between the CNTR and GOES
 921 simulations. (d) Ratio of O₃ difference between EMIS_BVOC and GOES simulations to O₃
 922 difference between CNTR and GOES simulations, i.e., $\Delta O_3(EMIS_BVOC - GOES)/\Delta O_3(CNTR -$
 923 $GOES)$. Note that the grids that have considerable O₃ difference between CNTR and GOES
 924 simulations (> 1 ppb) are depicted in (d).

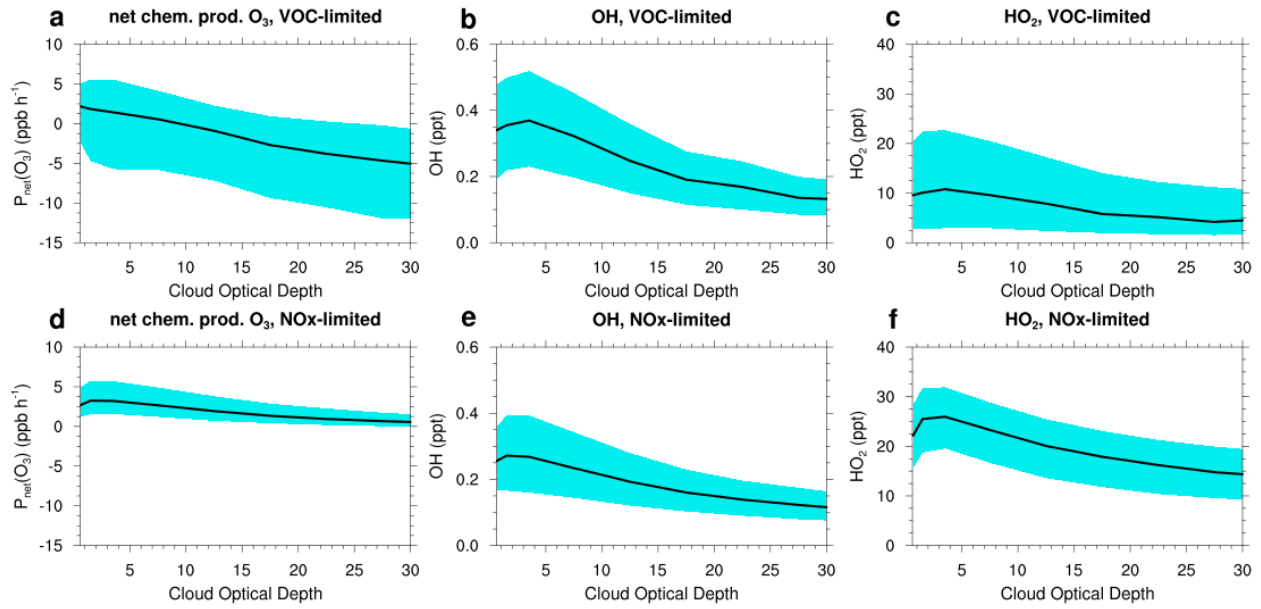


925

926 Fig. 7. (a) Probability density function of maximum daily 8-h average (MDA8) O₃ bias (model
 927 value minus observation value) for VOC-limited regime under cloudy sky conditions defined
 928 with COD threshold of 20. (b) Same as (a), but for NO_x-limited regime. (c) Median values of
 929 MDA8 O₃ bias with respect to COD threshold in the CNTR simulation (solid lines with cross
 930 marks) and in the GOES simulation (dashed line with triangles) for VOC-limited (purple color)
 931 and NO_x-limited regimes (green color). (d) Difference in median values of MDA8 O₃ bias
 932 between the two simulations with respect to COD threshold (i.e., CNTR minus GOES).

933

934



935

936 Fig. 8. (a) Net chemical production of O_3 , (b) OH concentration, and (c) HO_2 concentration with
 937 variations of cloud optical depth for VOC-limited regime. The black line indicates the median
 938 and cyan shading indicates the 25 and 75 percentiles. Similar variables are shown for the NO_x -
 939 limited regimes (d, e, and f).

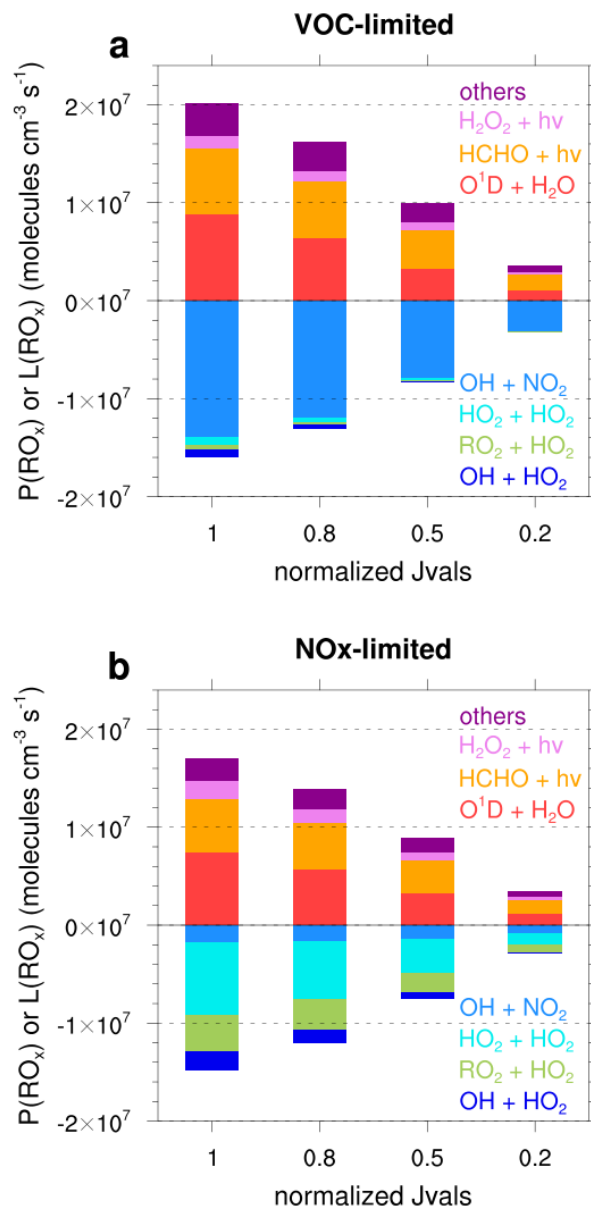
940

941

942

943

944



945

946 Fig. 9. Results of box modeling for production and loss rates of RO_x ($= \text{OH} + \text{HO}_2 + \text{RO}_2$)
 947 radicals. “Others” in the legend indicates the photolysis of VOCs and reactions between alkenes
 948 and O_3 . The value of 1 of normalized Jvals on x -axis indicates the photolysis rates for clear sky
 949 conditions.

950